

CRANFIELD UNIVERSITY

Pau Gomà Golanó

MODAL ANALYSIS OF AN OPTICAL TEST SYSTEM
FOR METRE-SCALE OPTICS

SCHOOL OF AEROSPACE, TRANSPORT AND
MANUFACTURING
MSc in Manufacturing Technology and Management

MSc THESIS
Academic Year: 2015 - 2016

Supervisor: Dr Renaud Jourdain
Co-supervisors: Dr Luca Zanotti Fregonara and Jonathan Abir
September 2016

CRANFIELD UNIVERSITY

SCHOOL OF AEROSPACE, TRANSPORT AND
MANUFACTURING
Manufacturing Technology and Management

MSc THESIS

Academic Year 2015- 2016

Pau Gomà Golanó

Modal Analysis of an Optical Test System
for Metre-Scale Optics

Supervisor: Dr Renaud Jourdain

Co-supervisors: Dr Luca Zanotti Fregonara and Mr Jonathan Abir

September 2016

This thesis is submitted in partial fulfilment of the requirements for the degree of MSc in Manufacturing Technology and Management.

© Cranfield University 2016. All rights reserved. No part of this publication may be reproduced without the written permission of the copyright owner.

ABSTRACT

The next generation of earth based large telescopes, such the European Extremely Large Telescope (E-ELT) targeted for 2024, will boost the space exploration and the search for other life in the universe. The primary mirror of the E-ELT will reach up to 39 metres of aperture. It will be composed by hundreds of 1.5 m corner to corner hexagonal mirror segments. The surface from of these segments need to be manufactured at nanometre level. The bottleneck on the manufacturing process of these segments is the figuring. Indeed, the iterative measurements and correction is extremely time consuming.

To address the measurement issue, the Precision Engineering Institute of Cranfield University has developed a unique Optical Test System (OTS) for metre-scale optics. It is a four metre structure that uses the latest technology in laser interferometry to assess the surface topography of the optical component. This result is used to feed the de-convolution algorithm used for moving the plasma tool that etch the surface. The motion system of on the figuring machine enable to precisely remove atomic layer of material on well-defined regions of the surface.

This thesis explores both the characterization and the scaling up process of the optical test system (OTS) designed for the figuring process mentioned above. In order to do so, a finite element model was created using ANSYS Mechanical APDL and the numerical modal analysis was performed. Then, the structure was tested through an experimental modal analysis (EMA), using the software LMS Test.LAB. The modal parameters of the structure (natural frequencies, damping and mode shapes) were obtained.

A correlation with less than 5% discrepancy was achieved between the modelling and numerical approaches. This small discrepancy was achieved after numerous model refinement iterations. However, this correlation enabled to validate the numerical model. Based on this broad set of results, a transmissibility study between the points of interest (test piece and the

interferometer) was carried out. Results showed the influence that different modes may have on the performance of the OTS.

Finally, recommendations were elaborated for addressing the scaling up of the OTS that is made of bolted aluminium extrusion profiles. Reinforcing the base structure and stiffening of joints are the two main recommendations for scaling up the OTS.

Keywords:

Experimental Modal Analysis, FEA, Vibrations, Correlation, Interferometry

ACKNOWLEDGEMENTS

I would first like to thank to my supervisors, Dr Renaud Jourdain, Dr Luca Zanotti Fragonara and Mr Jonathan Abir, for their unconditional advice and discussions along the development of this project, to each of them for their particular contribution.

I would also like to thank to the Cranfield University Precision Engineering Institute laboratory staff, for their help on every issue during the experimental work.

Finally, I would like to express my gratitude to my family, for their support throughout my years of study; and to Gemma, for her encouragement throughout the progression on this project and academic year.

TABLE OF CONTENTS

ABSTRACT	i
ACKNOWLEDGEMENTS.....	iii
LIST OF FIGURES.....	vii
LIST OF TABLES	x
LIST OF EQUATIONS.....	xi
LIST OF ABBREVIATIONS	xii
1 INTRODUCTION.....	13
1.1 Next Generation of Earth Based Telescopes	13
1.2 Metre-scale Optics Manufacturing	14
1.3 The Optical Test System (OTS).....	16
1.4 Aim & Objectives.....	18
1.5 Thesis Structure.....	18
2 LITERATURE REVIEW	19
2.1 Interferometry	19
2.1.1 Phase errors in PSI	20
2.1.2 Spatial-carrier phase-shifting (SCPS).....	21
2.1.3 DynaFiz™ interferometer	21
2.2 Optical Test Systems for Large Scale Optics.....	22
2.2.1 Sources of environmental error	22
2.2.2 Minimizing the effect of vibrations	23
2.3 Mechanical Vibrations.....	24
2.3.1 Analytical vibration Analysis	25
2.3.2 Modal analysis	26
2.4 Guiding rules for modelling the OTS.....	28
3 METHODOLOGY	30
4 FINITE ELEMENT MODEL AND ANALYSIS	32
4.1 Finite Element Modelling of the OTS	32
4.1.1 Assumptions of the model	32
4.1.2 Model Data	33
4.1.3 Model refinements.....	34
4.2 Modal Analysis Results.....	36
4.2.1 Modes and natural frequencies	37
5 EXPERIMENTAL MODAL ANALYSIS	41
5.1 Modal Testing Equipment	41
5.1.1 Equipment verification	42
5.1.2 Structure Preparation	43
5.2 Test Planning.....	43
5.3 Experimental Setup.....	45
5.3.1 Acquisition procedure.....	45
5.4 Modal Parameter Estimation.....	45

6 RESULTS CORRELATION	50
7 TRANSMISSIBILITY STUDY	53
8 RECOMMENDATIONS AND FURTHER WORK FOR ENHANCING THE OTS PERFORMANCE	60
8.1 Reinforcing the base structure	60
8.1.1 Adding base supports.....	60
8.1.2 Reducing the free length of the tower.....	61
8.2 Stiffening the square storeys	61
8.3 Placing the structure on an insulating mat	62
8.4 Structural material choice	62
9 CONCLUSIONS	64
REFERENCES.....	66
APPENDICES	71

LIST OF FIGURES

Figure 1. Artist recreation of the European Extremely Large Telescope (E-ELT), with a 39-metres primary mirror. Obtained from the European Southern Observatory web page (www.eso.org).....	14
Figure 2. Rapid manufacturing process for large scale mirror segments, extracted from [1].....	15
Figure 3. The OTS on the Precision Engineering Institute laboratory, at Cranfield University.	16
Figure 4. Interferometer and its support structure.	17
Figure 5. Positioning plate and the test piece on top.....	17
Figure 6. Schematic of a Fizeau type interferometer implementing PSI.....	19
Figure 7. Numerical simulations of the RMS phase error in different PSI algorithms vs the normalized vibration frequency. From [15].....	20
Figure 8. ZYGO® DynaFiz™ dynamic interferometer system.....	21
Figure 9. Optical test system of the Steward Observatory [30].....	23
Figure 10. FE Model of a cathead transmission tower. Extracted from [37].	28
Figure 11. On the left, the element BEAM188 geometry. On the right, the element SHELL181. Extracted from [35]	29
Figure 12. Methodology block diagram	31
Figure 13. Detail of the bolted connection between the base, one vertical pillar and the lower platen (in red).....	32
Figure 14. Detail of the bolted joints between rods, just one node in the model.	32
Figure 15. Section schematics of the OTS profiles.....	33
Figure 16. Detail of the interferometer modelling. In pink, rigid links between elements.....	35
Figure 17. Rubbery levelling foot supporting the OTS. Superimposed, its modelling approach as three linear springs.	35
Figure 18. Finite element model of the OTS (left) and CAD illustration (right)..	36
Figure 19. Result convergence when reducing the element size.	37
Figure 20. First mode, bending about the Y axis, at 4.37 Hz. In blue, the deflected shape.	38
Figure 21. Second mode, bending about the X axis, at 6.43 Hz. In blue, the deflected shape.	38

Figure 22. Third mode, the vertical oscillation, at 22.06 Hz. In blue, the deflected shape.	39
Figure 23. Fourth mode, torsion of the tower, at 30.16 Hz. In blue, the deflected shape.	39
Figure 24. Local mode of the second floor crossed beams, at 42.81 Hz.	40
Figure 25. The 16 channel dynamic data acquisition (LMS SCADA III).	41
Figure 26. The two types of accelerometer used for the tests, both ICP® PCB Piezotronics.	41
Figure 27. Impulse force test hammer, with interchangeable rubber tip.	41
Figure 28. Impulse hammer response curves.	42
Figure 29. Qualitative comparison of the FRF of the four accelerometers in their X axis as a verification procedure.	43
Figure 30. Accelerometers locations (green dots) and impact directions (red arrows) on the LMS Test.Lab geometry definition.	44
Figure 31. Experimental Setup with equipment identified.	44
Figure 32. Stabilization chart with stable real poles selected.	46
Figure 33. Auto-MAC matrix of the first set extracted.	47
Figure 34. Auto-MAC matrix of the final set of modes.	48
Figure 35. Mode shape at 70.6 Hz, mode 11 of the measured set. Note angular distortion of the square storeys of the tower.	49
Figure 36. Measured and predicted natural frequencies.	50
Figure 37. Graphically paired modes. Frequency, damping and discrepancy between the model (left side) and the experimental results (right side).	52
Figure 38. Cartesian coordinate systems for computing transmissibility functions.	53
Figure 39. On the left, the accelerometer on the test piece centre. In black, the coordinate system for computing the transmissibility, X-Y is the test piece plane. On the right, the accelerometer on the interferometer's case.	54
Figure 40. Transmissibility functions between the test piece and the interferometer.	55
Figure 41. Transmissibility functions between platens.	57
Figure 42. Comparison of the two transmissibility functions in X direction.	58
Figure 43. Comparison of the two transmissibility functions in Y direction.	58
Figure 44. Comparison of the two transmissibility functions in Z direction.	59

Figure 45. Base reinforcement schematic. In green, the added support below the main pillars of the OTS. 60

Figure 46. Surrounding base structure (in green) and buttress profiles (in blue). 61

Figure 47. OTS square cross-section. In green, reinforcement rods. 61

Figure 48. OTS without levelling feet over a rubber mat. 62

LIST OF TABLES

Table 1. Section properties for the three profiles of the OTS.	33
Table 2. Frequencies and mode shapes obtained with the FEA.	40
Table 3. Modal parameters estimated from the EMA.	48
Table 4. Correlation in Frequency summary.....	51
Table 5. Aluminium and steel mechanical properties and specific stiffness.	62

LIST OF EQUATIONS

Equation (2-1).....	25
Equation (2-2).....	26
Equation (2-3).....	26
Equation (2-4).....	26
Equation (2-5).....	27
Equation (2-6).....	27
Equation (2-7).....	27
Equation (2-8).....	28
Equation (7-1).....	53
Equation (7-2).....	54
Equation (7-3).....	54
Equation (7-4).....	54
Equation (7-5).....	54
Equation (8-1).....	61

LIST OF ABBREVIATIONS

ADC	Analogue-to-Digital Converter
APDL	ANSYS Parametric Design Language
CAD	Computer Aided Design
CoG	Centre of Gravity
DOF	Degree Of Freedom
E-ELT	European Extremely Large Telescope
EMA	Experimental Modal Analysis
FEA	Finite Element Analysis
FEM	Finite Element Method
FRF	Frequency Response Function
GMT	Giant Magellan Telescope
MAC	Modal Assurance Criterion
MPE	Modal Parameters Estimator
OTS	Optical Test System
PSI	Phase Shifting Interferometry
RMS	Root Mean Square
ROC:	Radius of Curvature
SCPS	Spatial-Carrier Phase-Shifting interferometry
TMT	Thirty Metre Telescope
ULE	Ultra-Low Expansion
X	X axis of the Cartesian coordinate system
Y	Y axis of the Cartesian coordinate system
Z	Z axis of the Cartesian coordinate system

1 INTRODUCTION

1.1 Next Generation of Earth Based Telescopes

Humankind has always been marvelled by the vastness of the Universe, and has continually pursued answers to the questions it presents. This ambition has been the driver for multiple discoveries and technological developments during history.

Telescopes, as the fundamental instrument in astronomy, play a key role enabling the advance of science and pushing technological development. In a manner, each breakthrough in telescope technology has brought with it a new scientific discovery. It happened with Galileo, applying new capability on fabricating glass lenses for building a new telescope with which he discovered Jupiter's moons, which supported largely the Copernican model. After that, Newton, Foucault and many others have followed this pattern [1], [2].

Nowadays, modern science is eager to answer fundamental questions for its development. Some of these questions are the study of the very beginning of the Universe and the processes that took place, the relationship between matter (dark matter and dark energy), or the direct measurement of the Universe size and its accelerating or decelerating growth. On the other hand, much effort is placed on the search for planets placed on the habitable zones of stars, where other forms of life may be possible [3]. These next scientific discoveries require, as history tell us, the next generation of equipment. For this purpose, the design of the next generation of telescopes has already started.

Extremely Large Telescopes (ELTs) are ground-based telescopes with an aperture diameter between 20 and 100 m for observation in the ultraviolet, visible and near infrared wavelengths. They are expected to show us a completely new horizon into the Universe. There are three main projects founded that are on their way through design or even to advanced stages on manufacturing. They are the Giant Magellan Telescope (GMT) of 24.5 metres [4], the Thirty Metre Telescope (TMT) of 30 metres [5] and the European Extremely Large Telescope (E-ELT) at 42 metres of aperture [1], [6], [7].

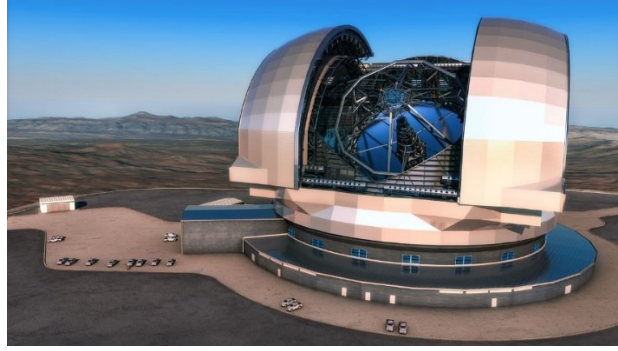


Figure 1. Artist recreation of the European Extremely Large Telescope (E-ELT), with a 39-metres primary mirror. Obtained from the European Southern Observatory web page (www.eso.org).

A baseline in all the ELTs is the segmentation of the primary mirror through multiple smaller mirrors. Their apertures are not feasible if they are done in one piece (monolithic), in terms of manufacturing, measurement and transportation. The segmentation of the primary mirror bring with it many optical challenges, but it has been proved to be effective during the last decades by the Keck telescopes (two telescopes with a primary mirror formed with 36 hexagonal segments forming a 10.2 m diameter primary mirror) and other telescopes [2].

Different strategies has been taken for the segmentation of the primary mirror. On one hand, GMT has adopted a design with 7 segments, each one of 8.4 m on diameter. On the other hand, TMT and E-ELT have chosen a deliberately equal and much smaller hexagonal segment size of 1.45 m, requiring 492 and 984 segments for the TMT and E-ELT respectively [1]. These figures certainly present a supply challenge on the manufacturing point of view, requiring the shift into mass production of extremely accurate metre-scale optics. Various research and industry groups are addressing this challenge.

1.2 Metre-scale Optics Manufacturing

The demand for metre-scale optics will scale up during the next decade, boosted for the different ELTs projects and other industries such electronics or energy [8]. To address this high demand, new manufacturing routes are required.

The Precision Engineering Institute at Cranfield University has been addressing this issue for last decades, developing a process chain to manufacture metre-scale optics in a much faster and efficient way than current methods. The process is divided in three discrete stages with dedicated machines for each one. The target on the horizon is <10 nm RMS form accuracy in less than 10 hours for metre-scale optics, a challenge when current technologies may take more than 100 h for the same specifications [9], [10].

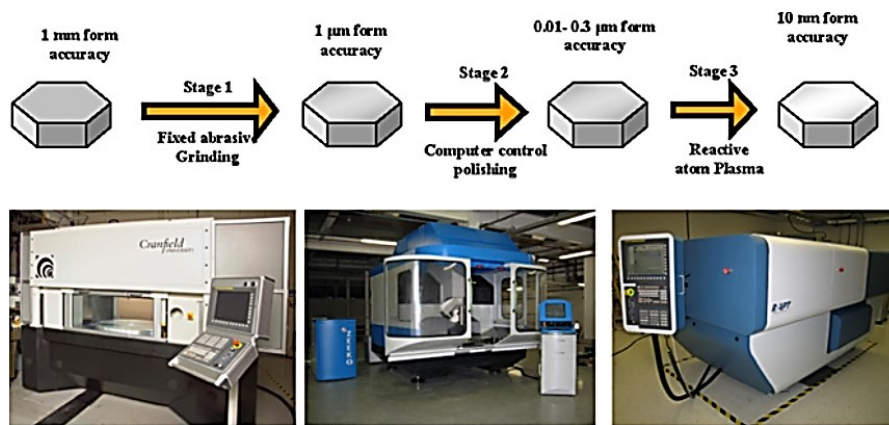


Figure 2. Rapid manufacturing process for large scale mirror segments, extracted from [1].

The manufacturing chain is composed with the three stages: grinding, polishing and plasma figuring. The first stage, grinding, is performed by the Cranfield BoX ultra-precision grinding machine. BoX was designed with a high static and dynamic stiffness loops to achieve ‘free form’ optical surfaces. This will reduce the time on subsequent manufacturing steps dramatically [11]. Then, the second stage is a polishing process, carried out with a Zeeko[®], an ultra-precision polishing commercial machine.

The last step of the manufacturing process is the optical finishing, an iterative process of measuring and figuring until the desired specifications are met. This stage has been always the bottle neck of the whole process. There are different techniques that address this step, basically divided in energy beam figuring (particles, laser or plasma) or mechanical and chemical polishing. Progressively, energy beam figuring techniques are growing into an essential fabrication technique for optical manufacturing chain.

In this direction, Cranfield University is developing a Plasma Figuring technology. This technology, first presented in [12], was patented by RAPT technologies in 2001 [13]. Cranfield University in partnership with RAPT technologies developed the second generation of plasma figuring machines named Helios 1200. Nowadays the Precision Engineering Institute research team continue doing strong research in this field [10].

The plasma figuring is an iterative correction process that enables to correct form errors. Plasma figuring requires measurements of the optical surfaces at nanometre level. Then this measurement capability is fundamental, since it provides critical information for the each plasma figuring iteration. In other words, the manufacturing metre-scale optics requires dedicated metrology system. This is the reason why the Precision Engineering Institute has developed a novel optical test system.

1.3 The Optical Test System (OTS)

The Optical Test System (OTS) is the unique optical metrology station for metre-scale optics of the Precision Engineering Institute in Cranfield University. The system and its characteristics will be soon presented in a journal paper [14].

The OTS, see Figure 3, is a four and a half metres tall tower, constituted by bolted aluminium extrusion profiles. The main elements are the interferometer –on the top of the tower– and the optical test piece on the bottom, which are hold by aluminium platens. It was designed and build to fulfil the need of the plasma figuring process. The OTS enables to measure metre-scale optics at high accuracy. Also the design is versatile and low cost.

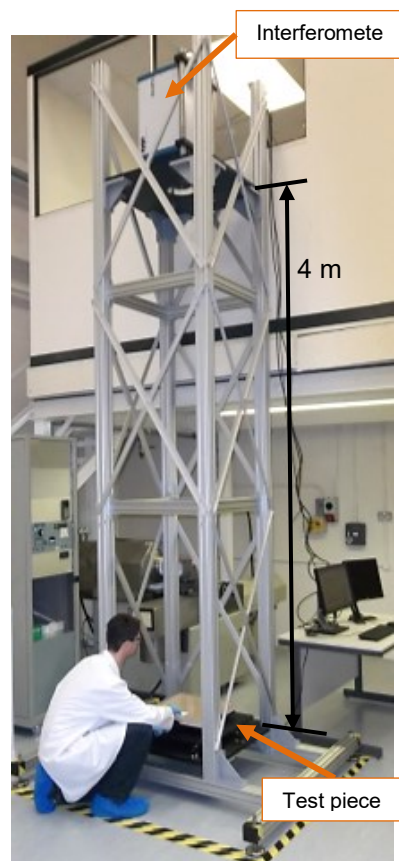


Figure 3. The OTS on the Precision Engineering Institute laboratory, at Cranfield University.

Furthermore, the OTS plays a key role as a technology demonstrator. In a near future, the Precision Engineering Institute aims to scale up the OTS and build a metrology system that is able to measure larger optics with larger radius of curvature (ROC). For example, the ROC of E-ELT mirrors is 84 m. This way, the Cranfield manufacturing chain capability will be complemented with a dedicated and bespoke OTS that will map the errors of the optics in order to feed it back to the plasma figuring machines.

Some of the advantages of the OTS design is that it can be assembled quickly, the footprint on the workshop is minimum and it can be adapted in order to test a large variety of optics and test pieces.

In more detail, the OTS uses interferometric techniques to perform a variety of optic measurements. It is equipped with a high performance, vibration insensitive interferometer on the top, which enables the use of a less stiff and isolated structure, resulting in a cheaper system. The interferometer is held by a support structure attached on the upper platen of the structure (see Figure 4).



Figure 4.
Interferometer and its support structure.

On the bottom of the tower, there is a positioning plate which enables fine-tuning in five degrees of freedom of the test piece position, three translations plus two tilts (see Figure 5). The test piece is supported by the positioning plate, on top of a thin foam that works as a vibrations insulator.



Figure 5.
Positioning plate and the test piece on top.

The structure is built based on commercially available aluminium extrusion profiles. The parts are bolted together which provide an easy way of transportation and assembly. The structure is supported by five rubber insulating levelling feet.

Back in 2015, the OTS was investigated to determine the effect of various parameters and external environmental effects into the measurement performance. Today in 2016, this work underpins the previous investigation by providing a study of the vibration characteristics of the OTS, through a modal analysis. This work enabled a deeper understanding of the mechanical structure and the design parameters. The influence of these parameters is discussed in the light of scaling up the OTS.

1.4 Aim & Objectives

The aim of this project is to improve the measurement capability of the Precision Engineering Institute by exploring the vibration characteristics of its unique Optical Test System (OTS), through both a numeric and experimental approach. In order to successfully accomplish the aim of the project, five objectives were set:

- Create a Finite Element model of the OTS and carry out a Modal Analysis.
- Carry out an Experimental Modal Analysis of the OTS structure.
- Correlate the results from both analysis and validate/update the model.
- Identify the effects that different vibration modes have on OTS through a Transmissibility study.
- Provide recommendations for scaling the OTS up.

1.5 Thesis Structure

In the introductory chapter -**Chapter 1**- the context, drivers and the aim of the project are presented. **Chapter 2** presents relevant literature and some theoretical notions of the topics involved along the thesis. **Chapter 3** declares the methodology followed during the development of this work. **Chapter 4** shows the finite element modelling approach and the analysis with the Finite Element Analysis (FEA) software. **Chapter 5** defines the experimental work carried out and the results obtained. **Chapter 6** presents the correlation of the results from the two approaches and **Chapter 7** the study of the influence of each mode on the system. **Chapter 8** provides recommendations for scaling up the OTS. Finally, **Chapter 9** concludes the thesis.

2 LITERATURE REVIEW

The purpose of this chapter is to introduce readers to the topics treated afterwards and to obtain valuable information from relevant literature.

2.1 Interferometry

Metrology is a basic pillar on the optics fabrication industry. For large optics, interferometric techniques are the most used on metrology systems.

Interferometry is a technique based on the interference phenomena that occur between waves, in this particular case light. The interferometer is the instrument that creates and analyses the interference patterns or fringes. The interference between a reference wavefront and the test optics wavefront provide the basis for precisely measuring different parameters of the optical parts.

One of the major techniques is Phase Shifting Interferometry (PSI) [15, Ch. 14]. PSI is based on the introduction of a time-varying phase shift between the two interfering wavefronts at a certain frequency. This derives in a temporary variation of the irradiance –as a magnitude of interference– received at each point of the sensor, a pixel of the interferometer’s camera. The desired phase shift is introduced by a small mechanical movement of the reference surface, which is driven by a piezoelectric transducer (PZT). Figure 6 shows a schematic of this configuration on a Fizeau type interferometer [15, Ch. 1].

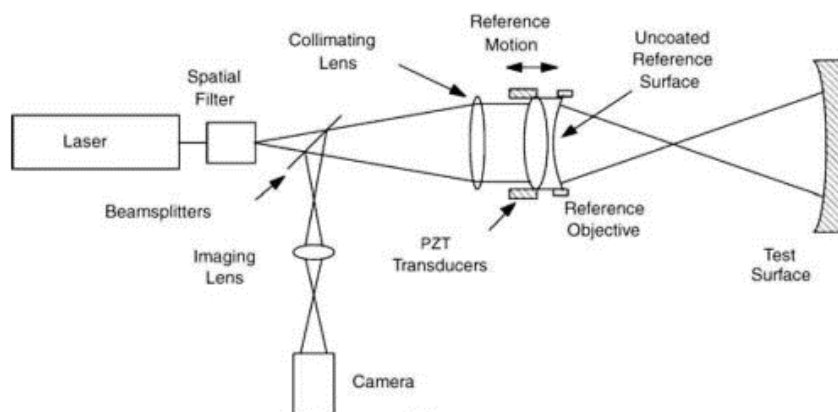


Figure 6. Schematic of a Fizeau type interferometer implementing PSI.

2.1.1 Phase errors in PSI

The nature of PSI introduces a time-dependent acquisition, since several images are taken at different instants, which is prone to be affected by other time-dependent phenomena. The two major phenomena affecting PSI performance are vibrations and air turbulences.

Vibration introduce an unknown phase error that is added to the phase shift, which is then traduced to an error on the measurements. Other errors are due both to air temperature changes and air motion. Indeed, air temperature and motion affect its refractive index. Consequently, the wavefront is disturbed.

Since 90's this issue has been addressed by the introduction of new algorithms and methods [16]–[19]. Bespoke algorithm enabled to reduce the effect of vibrations up to 1-2 orders of magnitude. De Groot published in 1995 [20] a rigorous mathematical derivation of the vibration errors affecting the phase detection in PSI. In 1996, de Groot and Deck [21] performed numerical simulations of different PSI algorithms and found their sensitivity to vibrations as RMS of the measurement error. They pointed out the relationship between the phase error and the ratio between vibration frequency and sampling frequency (shifting frequency). The largest errors occur below the sampling frequency and in particular in the odd harmonics of this frequency (Figure 7).

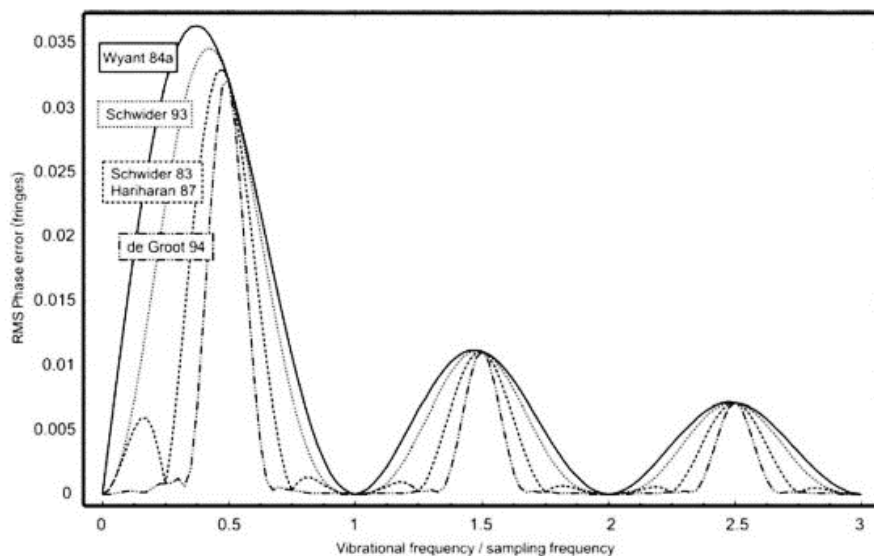


Figure 7. Numerical simulations of the RMS phase error in different PSI algorithms vs the normalized vibration frequency. From [15].

The problem with vibrations in PSI is well known and steps have been done towards the mitigation of their effects. Nevertheless PSI are likely to perform poorly when the environmental noise conditions are severe, the interferometer and test piece are in different metrology platforms, or the optical path length is few metres long [22]. Fortunately, new analysis techniques, called spatial methods, solved this issue when higher resolution cameras became available.

2.1.2 Spatial-carrier phase-shifting (SCPS)

The essence of spatial-carrier phase-shifting -instantaneous interferometry- is to compute the phase difference at each pixel with the irradiance variation along the space rather than time. Given that the variation between fringes follows a sinusoidal wave, the phase in one pixel can be calculated taking advantage of the irradiances of the adjacent pixels [23], [24].

In this way, with just one interferogram the phase at each pixel can be detected. Taking into account that the exposure time of one camera frame can be less than one millisecond, environmental effects such vibrations and air turbulence are effectively minimized.

However, vibration insensitive interferometers have also some drawbacks such less accuracy than some PSI algorithms, mainly due to higher sensitivity to noise in irradiance data [14]. This is the reason why PSI is always desirable, if the environmental conditions allow it.

2.1.3 DynaFiz™ interferometer

The interferometer mounted on the Optical Test System studied here is the DynaFiz™ by ZIGO® [25]–[27] (Figure 8).

This instrument is a laser based Fizeau-type interferometer that includes traditional PSI acquisition and dynamic acquisition, with vibration insensitive algorithms such SCPS.



Figure 8. ZYGO® DynaFiz™ dynamic interferometer system.

Its modular design enables the reference surface of the interferometer to be changed easily depending on the piece tested (i.e. reference flats, transmission spheres for convex and concave surfaces). This interferometer, and the majority of its kind, uses a helium-neon gas laser very precisely stabilized at a wavelength of 632.8 nm, with a coherence length greater than 100 m.

2.2 Optical Test Systems for Large Scale Optics

In the previous section, the vibration effects on interferometry were presented. This section focuses on both the types of environmental error that may affect an optical test system, and the different approaches used to minimize vibration effects in large optical test systems. The review could be useful when scaling the existing OTS up.

2.2.1 Sources of environmental error

In an optical test system for optics with large radius of curvature (ROC) like segmented primary mirrors, the test piece and the measurement system are separated many metres. Moreover, the level of accuracy (nanometres) and repeatability are challenging. In these conditions, environmental sources of error need to be either controlled or mitigated.

Air refractive index changes with temperature. This fact introduces a random error when the light crosses through several metres of air. These errors are minimized when averaging many measurements. In order to minimize this source of error, a large and temperature controlled environment must enable to secure a good mixing of the surrounding air [28, Ch. 4]. Another strategy is to contain the air between the test piece and the testing equipment with a shirt in order to maintain a constant air gradient, such in the testing tower of the REOSC laboratory [29].

The other main source of random error are vibrations. Even though, there are interferometric techniques -SCPS- that minimise the effects of vibrations, the accuracy of the measurements is expected to be lower compared to regular PSI. Then, if vibrations allow PSI, it is always the best option. That is the reason

why much care is taken in minimizing vibrations when designing an optical test system.

2.2.2 Minimizing the effect of vibrations

Different techniques are used to minimize vibration effects. Often they are combined to enhance the results. Stiffening, passive and active control are detailed hereafter.

- **Stiffen the structure**

The first approach for minimizing vibrations is following design guidelines like enhancing high static stiffness and minimizing thermal growth [14]. These design rules are applicable also to telescope structure designs. Stiff structure secures higher natural frequencies. An example can be found at the Sagem-REOSC facility. This company manufactured the primary mirrors of the VLT and GEMINI telescopes. Their facility includes a 35 m optical test system [29].

- **Passive vibration absorption**

A passive isolation system is desirable in order to prevent the transmission of the vibrations from the ground to the test system structure. This can be achieved by a seismic mass (cement foundation) or with insulating mount pads on the machine/structure.

The optical test system used for the primary mirrors of the GMT telescope [30] is a 24 m tower isolated from the ground through a suspended seismic mass. The foundation is supported by pneumatic supports that absorb the vibrations. This configuration allows the use of PSI even if the large distance exists between test piece and interferometer.

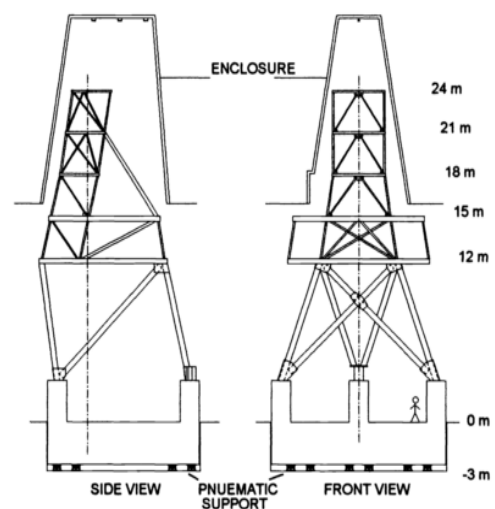


Figure 9. Optical test system of the Steward Observatory [30].

- **Vibration isolation: Active control**

Control techniques allow the mitigation of vibration in real-time, compensating their effects with actuators. The application on large structures is sometimes difficult. Nevertheless, it can be useful when compensating the vibrations on the interferometer or on the test piece when they are few metres away like in an OTS [31].

2.3 Mechanical Vibrations

This section focuses onto mechanical vibrations and reviews the modal analysis theory that underpins this work.

A mechanical vibration is defined as an oscillatory movement, periodic or not, of a system or part around an equilibrium state. Vibrations can be classified in different ways. One of them is through the energy source driving the system. The set of three bullet points hereafter highlights and details free vibrations, forced vibrations, and self-excited vibrations.

- Free vibrations: an impact (energy input) excites the system and the energy is dissipated through time with the damping of the system. An example can be an impact to a tuning fork.
- Forced vibrations: The energy source continually excites the system at a certain pace and the vibration of the system will depend on this exciter until it stops. An example can be a rotating machine at certain frequency.
- Self-excited vibrations: The system has available energy which it takes at its preferred pace. An example can be a wind instrument.

The Optical Test System -a static structure- is treated as a receiver of vibrations that come from many different sources. These vibrations, which somehow arrive at the OTS through the ground or air, provide the structure with an energy that will be transformed into its free vibration.

Each structure has their set of patterns of free motion, called modes of vibration. A mode can be described as an oscillatory movement of all the system at the same frequency -resonant or natural frequency-. Normally, the

motion of the structure is described as a superposition of modes. The analysis of the modes and resonant frequencies can give fundamental information about the dynamics of the system.

Forced vibration was also considered. For example, a big rotating machine near the OTS can potentially induce a strong vibration at a specific frequency. Then the energy would not be transformed to a free vibration at the natural frequencies of the system but the structure would be excited by force at frequency of the energy input. This possibility is out of the scope of this thesis, but could be further studied in the future.

2.3.1 Analytical vibration Analysis

The theoretical background of the vibration analysis and its application with the finite element method (FEM) is presented hereafter. A more concise review of the process can be found in [32].

The vibration analysis of a system always starts with the determination of its equations of motion. There are different methods to do that, but when dealing with many degrees of freedom, the Hamilton's Principle is the most suitable choice. It is expressed with the Lagrange's equations for a system with n degrees of freedom as

$$\frac{d}{dt} \left(\frac{\partial T}{\partial \dot{q}_i} \right) + \left(\frac{\partial D}{\partial \dot{q}_i} \right) + \left(\frac{\partial U}{\partial q_i} \right) = Q_i \quad i = 1, 2, \dots, n \quad (2-1)$$

where T is the kinetic energy, U is the strain energy (potential energy for a structure) and D is the dissipation of energy or damping. Q_i is the generalised force, equal to the work done by an external force when applying a unit displacement to the degree of freedom (DOF) displacement q_i .

In continuum mechanics, where the solids are considered deformable, each body is constituted by an infinite number of points with their degrees of freedom. Then the movement of the body needs to be described by a continuous function. The Rayleigh-Ritz method approximates a continuous displacement

with the sum of a finite number of equations. This enables the reduction of the Lagrange's equations to a matrix system

$$[M]\{\ddot{q}\} + [C]\{\dot{q}\} + [K]\{q\} = \{Q\} \quad (2-2)$$

where $[M]$ is the inertia matrix (or simply the mass matrix), coming from the kinetic energy, it is always positive defined. $[C]$ is the damping matrix extracted from the dissipation, and $[K]$ is the stiffness matrix extracted from the strain energy. Then $\{q\}$ is the vector of generalised displacements (as a function of time), and $\{Q\}$ is the vector of generalised forces (excitations).

In the Rayleigh-Ritz method, the displacement discretization is done along all the structure movement. This presents an issue when dealing with complex geometries. This issue is overcome with the use of the finite element displacement method. This method is based on the application of the Rayleigh-Ritz method but on a small discretized part of the geometry defined by nodes. The combination of these two methods enable the accurate vibration analysis of complex structures.

2.3.2 Modal analysis

The first analysis to understand the vibrational characteristics of a system is the modal analysis. A modal analysis enables to determine the natural frequencies of the system and the associated mode shapes. This analysis is performed solving the equation of motion as a free motion of the undamped structure,

$$[M]\{\ddot{u}\} + [K]\{u\} = 0 \quad (2-3)$$

where, now, the generalized coordinate is particularized as a nodal degree of freedom displacement $\{u\}$, a column vector $N \times 1$, N being the number of degrees of freedom. The solutions (N) of this system are described as

$$\{u\} = \{\phi\}e^{j\omega t} \quad (2-4)$$

which are harmonic displacements at a frequency ω . $\{\phi\}$ is the vector of amplitudes, normally referred as eigenvector. This equation implies the

movement of the whole system at a certain frequency. Combining equation 2-3 and 2-4, and simplifying result on

$$[[K] - \omega^2[M]]\{\phi\} = 0 \quad (2-5)$$

where the non-trivial solutions can be solved as a linear eigenvalue problem. Different methods are available to solve this problem; the solver chosen for the FE analysis carried out during this thesis operates with the Block Lanczos method [33], which is a variation of the original Lanczos method [34]. This method is suitable for large models with many constrain equations [35].

The solution is the set of eigenvalues λ , defined as $\lambda = \omega^2$. Then ω are the natural frequencies of the undamped system. If substituted on the equation 2-5 the corresponding mode shape, i.e. the eigenvector $\{\phi\}$ of each frequency, is found.

It is important to note that while natural frequencies are fixed figures, the eigenvectors are just relative values of the amplitude of the movement, and they do not represent the real displacement of the mode shape. In order to scale the vectors, they are usually normalized against the mass matrix as:

$$\{\phi_i\}^T[M]\{\phi_i\} = [I] \quad (2-6)$$

Another important and useful property of the eigenvectors is that they are orthogonal between them:

$$\{\phi_i\}^T[M]\{\phi_j\} = 0 \quad , i \neq j. \quad (2-7)$$

This property is the basis of the experimental assurance criterions, like the Modal Assurance Criterion (MAC), that can be used to check the validity of the modal vectors estimated from the measured frequency response functions extracted from a modal test [36].

The MAC is a scalar constant which shows the level of correlation between two modal vectors, $\{\phi_r\}$ and $\{\phi_s\}$:

$$MAC_{rs} = \frac{|\{\phi_r\}^T\{\phi_s\}|^2}{\{\phi_r\}^T\{\phi_r\}\{\phi_s\}^T\{\phi_s\}} \quad (2-8)$$

The MAC ranges between 0 (no similarity) and 1 (highly similar vectors). The MAC can be extended and used as an Auto-MAC, to validate one set of modal vectors, finding the correlation between them. This measure can highlight correlated modal vectors that could be at the end the same one. It can be used also to pair and correlate modal vectors extracted from an experimental test and a finite element analysis.

2.4 Guiding rules for modelling the OTS

This section presents briefly the FEA software used and some key pieces of information extracted from related literature. Also the element types used for modelling the OTS is discussed. The detailed modelling of the OTS and analysis is presented in detail in Chapter 4.

The FEA software used on this project was the ANSYS Mechanical APDL, *Release 16.2*. The decision on using this particular software was driven, first, by the availability of licences in the University, and secondly, by the large scripting capabilities which gave full control over the model and analysis.

In order to build the FE model of the optical test system effectively, similar studies were found and scrutinized.

A well-documented studies are the FEA modal analysis of electrical transmission towers [37]–[39]. These structures are normally built with steel rods bolted together in an intricate way and share large similarities with the OTS (see Section 1.3). Their modelling approach and assumptions are used as a guide when modelling the OTS. Some boundary conditions stated in this publications are:

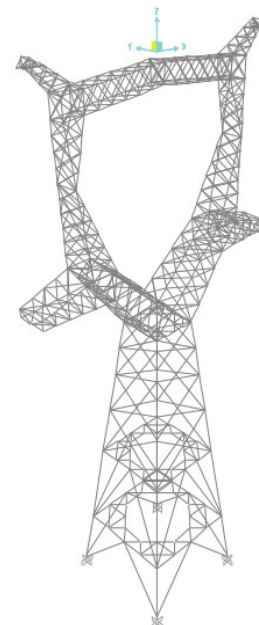


Figure 10. FE Model of a cathead transmission tower. Extracted from [37].

- The material is assumed linear elastic.
- The bolted connections between rods are assumed rigid.
- The length of the rods are assumed to be the distance between nodes.
- The rods are modelled with beam elements.
- The base supports are modelled as fixed.

With these concepts from literature and the capabilities of FEA software, the choice for the element type was made.

The aluminium extrusion profiles were modelled with the element BEAM188 available in ANSYS®. This element, based on Timoshenko beam theory, is suitable for modelling slender rods in a linear problem [35]. The element is defined in 3D between two nodes, with six degrees of freedom each one, three translations (x, y and z) and three rotations (around x, y and z axis). Moreover, it enables the definition of an arbitrary section, which was necessary when modelling the extrusion profiles of the OTS. Figure 11 shows the BEAM188 element.

For the aluminium platens, the element SHELL181 was chosen. Shell element provide an effective way of modelling bodies where one dimension is in comparison smaller than the other ones. This element is defined by four nodes, with six degrees of freedom each, and the thickness of the platen is specified (Figure 11).

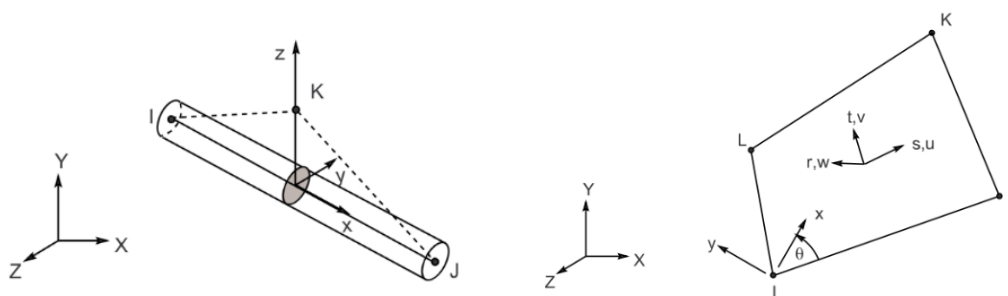


Figure 11. On the left, the element BEAM188 geometry. On the right, the element SHELL181. Extracted from [35]

3 METHODOLOGY

The methodology that this thesis follows is based on the model validation through the correlation of numerical (FEA) and experimental results [40].

The thesis work started first with background and relevant literature review, which set the theoretical foundations of the topics. Then a numerical model of the OTS was created using a FEA software package. A modal analysis of the numerical model was carried out. These preliminary FEA results were used to plan a modal testing. Prior undertaking the experimental work the entire OTS was scrutinized for finding loss fastenings. Thus, an Experimental Modal Analysis (EMA) was undertaken. As a matter of precaution, the set of accelerometer were mounted onto the OTS together and the response was analysed. Thus good practice were acquired and systematically implemented. The results' correlation between the two approaches (FEA and EMA) enabled the refinement of the model iteratively until an acceptable discrepancy. The model was then validated and the modal parameters of the structure were acquired. Based on this broad set of results, an experimental transmissibility study between the points of interest (test piece and the interferometer) was carried out. Results showed the influence that different modes may have on the performance of the OTS. Finally, conclusions were extracted and recommendations were elaborated for addressing the scaling up of the OTS.

The block diagram (Figure 12) illustrates this methodology.

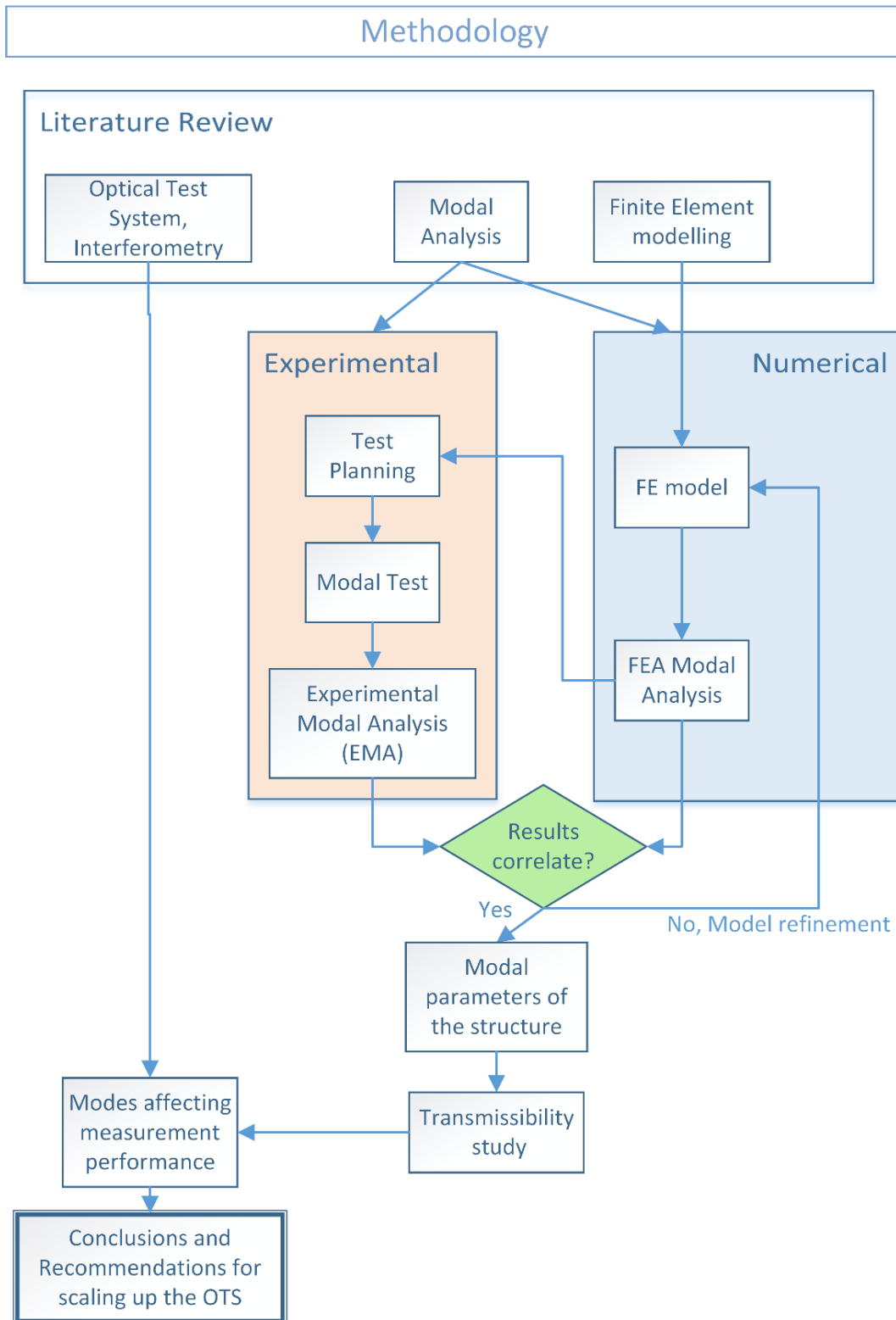


Figure 12. Methodology block diagram

4 FINITE ELEMENT MODEL AND ANALYSIS

This chapter presents the modelling approach that was used to create the finite element model of the optical test system (section 1.3). Then the results of the finite element model are analysed.

4.1 Finite Element Modelling of the OTS

4.1.1 Assumptions of the model

In order to model the OTS effectively some assumptions were made. Educated assumptions were based on the outcome of the literature review.

- The system was considered to have linear behaviour;
- The displacements induced by vibrations are small;
- The non-linear effects were neglected.

All the extrusion profiles were modelled as a unidimensional beam elements, passing through the central axis of them, and with the length between nodes or connections. These connections, which are actually bolted joints designed to restrain completely the movement of the parts, were modelled as a rigid joints between components (see Figure 14). The upper and lower platen were modelled as shells and they were connected with the beams in a rigid way (see Figure 13).



Figure 14. Detail of the bolted joints between rods, just one node in the model.



Figure 13. Detail of the bolted connection between the base, one vertical pillar and the lower platen (in red).

4.1.2 Model Data

The structure of the optical test system is based on three commercially available types of aluminium extruded profiles. Their dimensions and cross sections are presented in Figure 15.

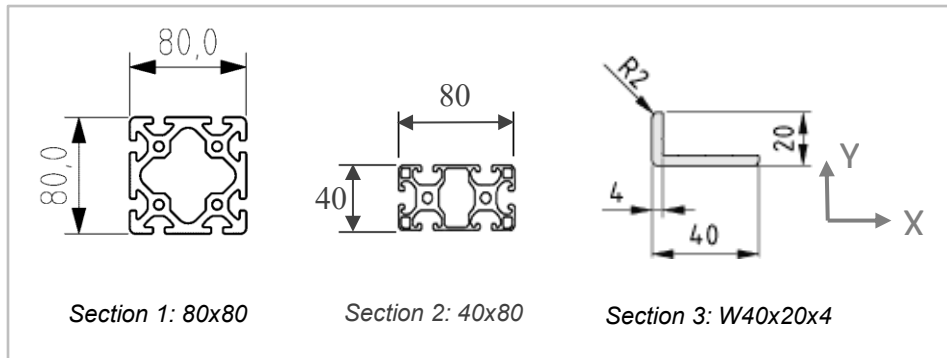


Figure 15. Section schematics of the OTS profiles.

As presented in the literature review chapter, these components were modelled with the element BEAM188, based on Timoshenko theory. This one dimensional element was defined on the longitudinal axis of the profiles. The section information was introduced on the BEAM188 element, with the properties presented in Table 1.

Table 1. Section properties for the three profiles of the OTS.

Profiles		SECTION 1: 80x80	SECTION 2: 40x80	SECTION 3: W40x20x4
Property	Units			
<i>Area</i>	mm ²	2.666	1.138	221
<i>I_{xx}</i>	mm ⁴	1.877.000	166.000	5.900
<i>I_{yy}</i>	mm ⁴	1.877.000	695.400	35.200
<i>I_t</i>	mm ⁴	1.284.000	99.400	1.100
<i>W_x</i>	mm ³	46.920	8.300	380
<i>W_y</i>	mm ³	46.920	17.380	1.400
<i>Mass/length</i>	kg/m	7,19	3,04	0,59

The upper and lower aluminium platens of the OTS were modelled with SHELL181, weighting 32 kg each.

The upper platen supports the weight of the interferometer and the structure that holds it, with a total mass of 67.8 kg. This equipment was first modelled as a lumped mass with the element MASS21, a one node element with mass [35].

The lower platen holds the positioning system, weighting a total of 16.6 kg, and the optical test piece, which was considered a typical ULE Glass sample of 420x420x40 mm with a weight of 15.6 kg. These masses were modelled also as a lumped mass on the centre of the platen.

The material of all the extruded profiles and platens is aluminium (6063A). The properties considered (obtained from www.matbase.com) were:

- Young's Modulus: = 75 GPa .
- Poisson ratio: = 0.33 .
- Density: $\rho = 2700 \text{ kg/m}^3$.

4.1.3 Model refinements

In this section, the main modelling refinements are presented. These refinements, as noted in the methodology -Chapter 3-, helped to fit the model closer to reality of the experimental results. Correlation between the experimental and FEA results is presented later on.

4.1.3.1 Interferometer modelling

The mass of the interferometer and its support reach up to 70 kg, which influences significantly on the structure dynamics. A proper representation of this mass distribution was necessary.

The interferometer support structure was modelled with beam elements (BEAM188), as the structure, with their correspondent section information. A point mass element (MASS21) was fixed on the centre of gravity of the interferometer. The command CERIG was used to generate constrain equations (rigid links) between the nodes on the support structure and the interferometer's centre of gravity (CoG). It was also used to connect the support structure to the shell (see Figure 16).

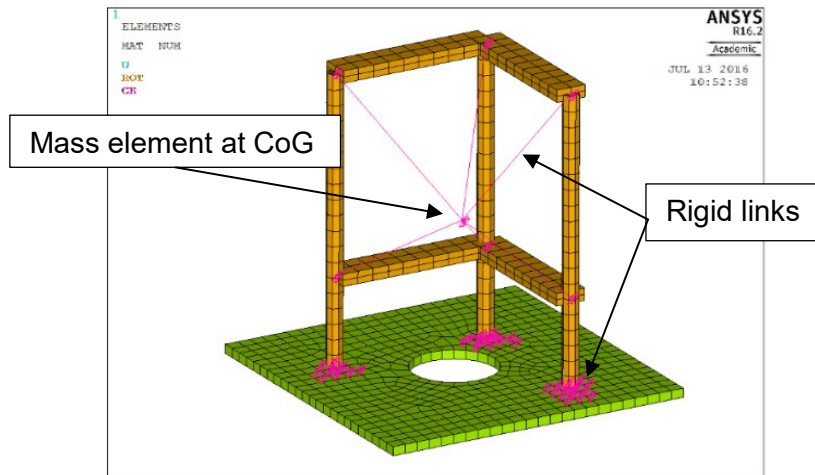


**Figure 16. Detail of the interferometer modelling.
In pink, rigid links between elements.**

This refinement helped to introduce the mass asymmetry on the structure and to better represent inertial forces transmission from the interferometer to the platen.

4.1.3.2 Boundary Conditions

Boundary conditions play a key role on any finite element model. They dictate how the model interacts with its environment.

The OTS is in contact with the ground in three main points through a vibration insulator support (see Figure 17). The set of three rubbery levelling feet work as a kinematic mount [41]. This design feature ensure the optimum constrain to hold and set the OTS. As a matter of safety, two additional rubbery levelling feet, ensure the stabilization of the structure in case of inclination.

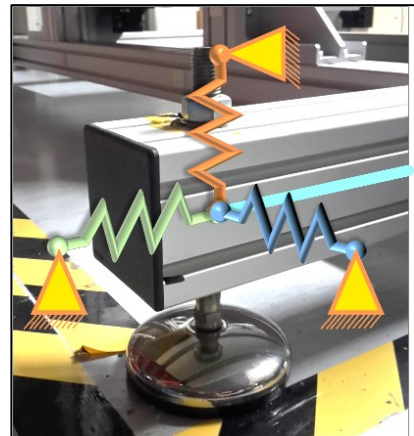


Figure 17. Rubberly levelling foot supporting the OTS. Superimposed, its modelling approach as three linear springs.

The nodes located close to the rubbery levelling feet were first clamped, constraining in all DOF. After the first correlation, it was seen that the supports played a key role in low frequency modes, where the vibration involved the

movement of all the structure. They were then modelled as three orthogonal linear springs, with the element type COMBIN14 [35]. One end of the spring was connected to the node in the structure, the other end was restrained in all DOF. Figure 17 represents schematically how the springs modelled the support.

After the model refinements, the final model was achieved and the modal analysis could start. Figure 18 shows the complete finite element model, composed by 2918 nodes and 2873 elements (at 40mm global element size).

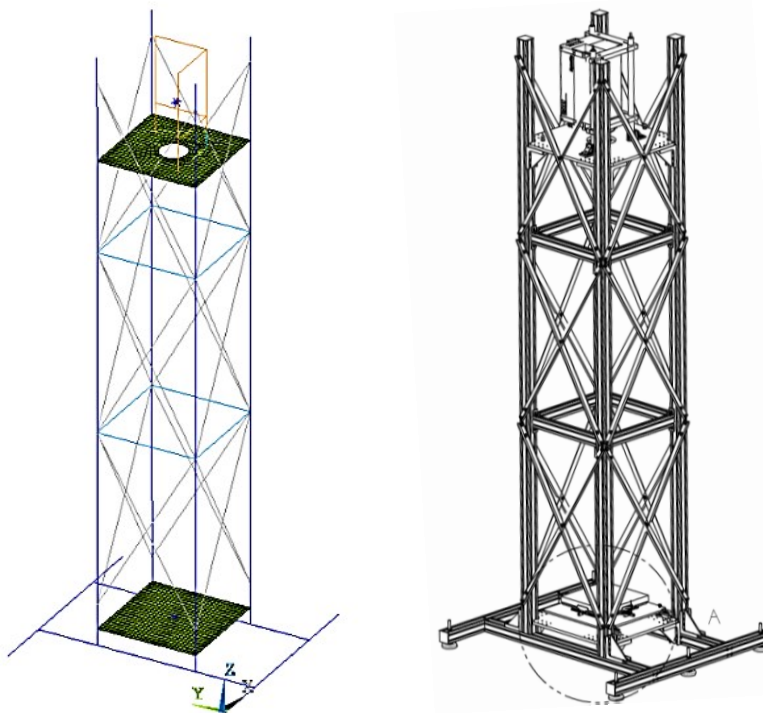


Figure 18. Finite element model of the OTS (left) and CAD illustration (right).

4.2 Modal Analysis Results

Once the model was completed, the geometry was discretized (meshed) with a global element size of 40 mm, which provided a good relation between accuracy and computational effort. Figure 19 illustrates the results convergence against the global element size at the beginning of the modelling steps (not final results).

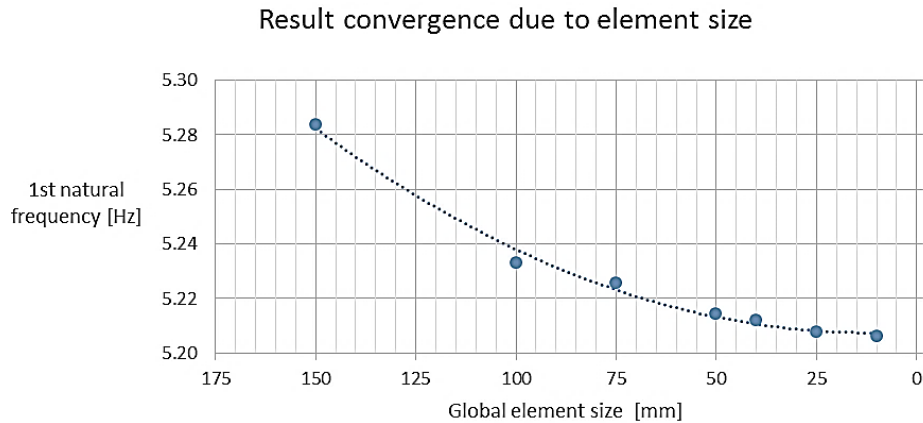


Figure 19. Result convergence when reducing the element size.

Following, the boundary conditions were applied on the model as explained on the previous section, with spring elements.

Finally, the solver for a modal analysis was set. As presented on the modal analysis theory review, in Section 2.3.2, the solver for this analysis face an eigenvalue problem, extracting the natural frequencies and mode shapes of the undamped system. The Eigen solver used was the Block Lanczos [35].

4.2.1 Modes and natural frequencies

In a structure such the OTS, composed by lots of different parts, a large number of modes exist (theoretically as many as degrees of freedom). Nevertheless, in reality just few of them are key to explain most of the dynamics of the structure.

Then one could argue the existence of local and global modes. Local modes involve the vibration of small parts of the structure and global modes involve a major mass participation of the overall. In this work it was chosen to focus on the global modes because they are known to dominate the dynamics of the structure and are considered more important.

Thus the calculation was set in the range 0 and 100 Hz. The first interpretation of these results showed that the mass participation of the modes over the frequency range was very low (99.9% cumulative mass fraction achieved with modes below 100 Hz).

The results of the modal analysis showed the first two modes at the frequencies of 4.37 Hz and 6.43 Hz. These two modes could be understood as the bending of tower structure along the X and Y directions. This results was expected because the structure has some degree of symmetry. Figure 20 and Figure 21 show the first and second modes respectively.

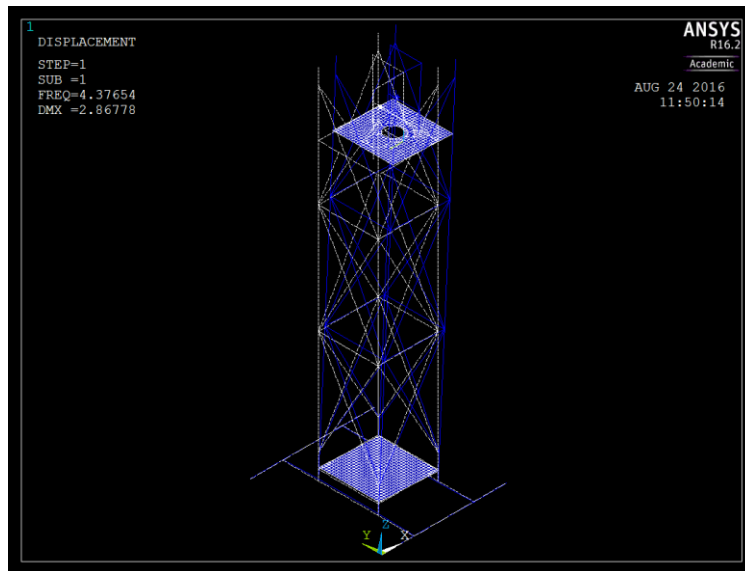


**Figure 20. First mode, bending about the Y axis, at 4.37 Hz.
In blue, the deflected shape.**

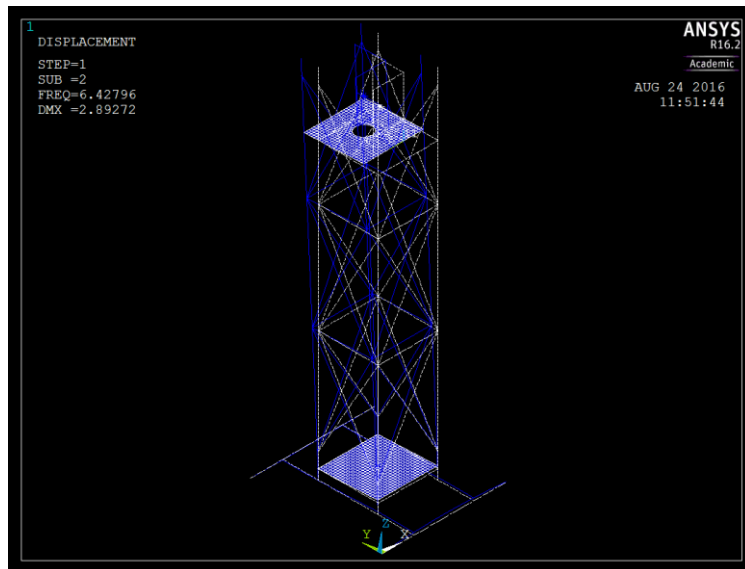


**Figure 21. Second mode, bending about the X axis, at 6.43 Hz.
In blue, the deflected shape.**

The third mode is the vertical oscillation at 22.06 Hz (Figure 22), that is due to the deflection of the bottom lower aluminium extruded profiles. The fourth mode is the torsion of the structure around its vertical axis at 30.16 Hz (Figure 23).

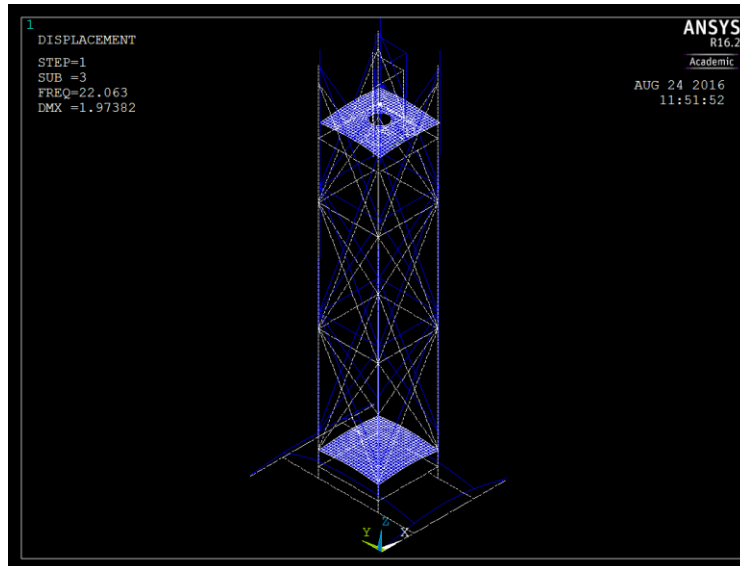


**Figure 22. Third mode, the vertical oscillation, at 22.06 Hz.
In blue, the deflected shape.**

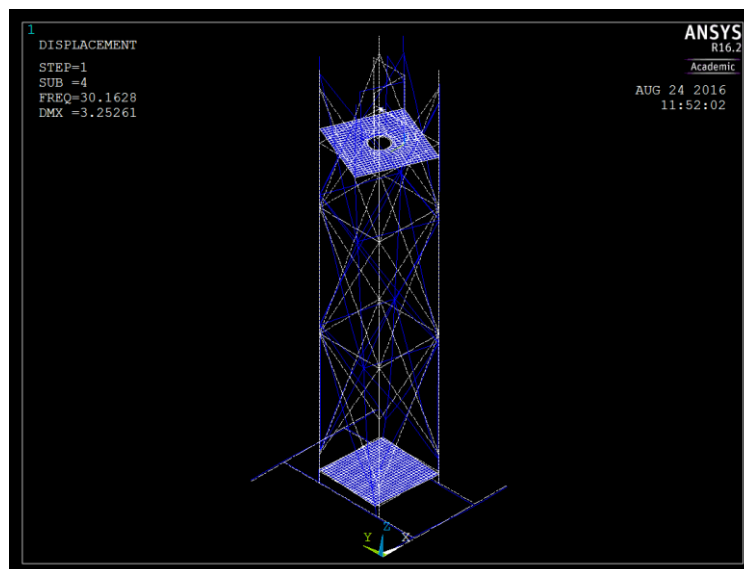


**Figure 23. Fourth mode, torsion of the tower, at 30.16 Hz.
In blue, the deflected shape.**

The set of four modes aforementioned are expected to dominate on the dynamic response of the structure. These modes characterise the lowest natural frequencies.

The following set of mode contains twelve local modes. They are characteristic of the different combinations of the first deflection modes of the crossed L shape aluminium extruded profiles. Results show that it exists four modes for each section of the OTS. Figure 24 shows one local mode (seventh on the system), which is the out-of-phase oscillation of the

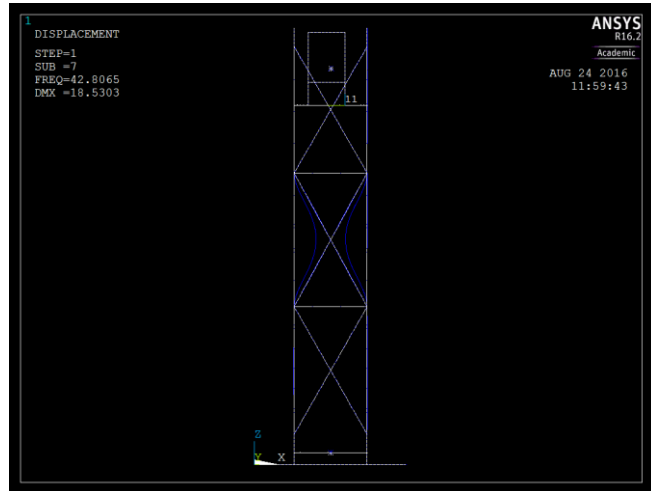


Figure 24. Local mode of the second floor crossed beams, at 42.81 Hz.

crossed rods on the second section. The resonance frequencies of these modes are very close, between approximately 40 and 50 Hz.

To conclude, Table 2 summarizes the final FEA results. A more complete graphical representation of the modes obtained can be found on the Appendix A.

Table 2. Frequencies and mode shapes obtained with the FEA.

	<i>Frequency f [Hz]</i>	<i>Type</i>
Mode 1	4.37	Bending on Y (Figure 20)
Mode 2	6.43	Bending on X (Figure 21)
Mode 3	22.06	Vertical (Figure 22)
Mode 4	30.16	Torsional (Figure 23)
Mode 5 - 18	40 - 50	Local Modes (Figure 24)
Mode 19	55.28	Platens oscillation out of phase
Mode 20	57.16	-
Mode 21	71.92	-
Mode 22	78.62	Platens oscillation in phase
Mode 23	83.34	Second torsional
Mode 24	93.66	-
Mode 25 - 51	95 - 115	Local Modes

5 EXPERIMENTAL MODAL ANALYSIS

This chapter presents the experimental methods and results.

5.1 Modal Testing Equipment

The equipment and software already available in the Precision Engineering Institute were used for carrying out the modal test. The equipment involved was:

- LMS SCADAS III, multichannel dynamic data acquisition (Figure 25),
- LMS Test.Lab software license,
- 4x Triaxial accelerometers (ICP® PCB Piezotronics models 2x 356A25 and 2x 356A24) (Figure 26),
- Impulse Force Test Hammer (ICP® PCI Piezotronics model 086D20) (Figure 27).



Figure 25. The 16 channel dynamic data acquisition (LMS SCADA III).



Model 356A25
25mV/g
1-5000Hz (+/- 5%)

Model 356A24
10 mV/g
1-9000Hz (+/- 5%)

Figure 26. The two types of accelerometer used for the tests, both ICP® PCB Piezotronics.



Figure 27. Impulse force test hammer, with interchangeable rubber tip.

The impulse force test hammer can mount various rubber tips in order to excite different frequency ranges. The harder the tip, the higher the frequency content of the response. The super soft tip was chosen to perform the experimental

modal analysis of the OTS, because a very low frequency range was of interest. Figure 28 shows the response curves for the different rubber tips available.

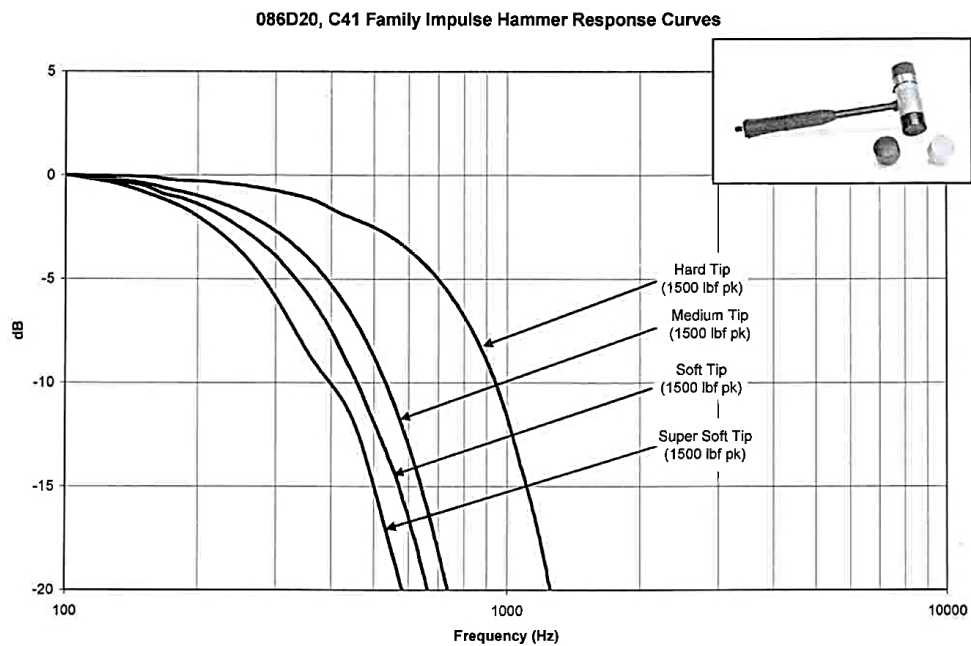


Figure 28. Impulse hammer response curves.

The complete equipment data sheets can be found in Appendix C.

5.1.1 Equipment verification

In order to check the correct operation of the accelerometers, cables and acquisition system in general, a brief qualitative experiment was carried out.

This task consisted in placing the four sensors on the OTS structure, at nearly the same point without touching each other. Then the structure was impacted in a different point, and the Frequency Response Functions of the X, Y and Z axis of the triaxial accelerometers were compared respectively.

The results showed similar responses of the accelerometers at the same resonant frequencies -peaks- (Figure 29), with less than 10% discrepancies in the magnitude on the worse cases. This verified the equipment and the adhesion method of the accelerometers; with thin layer of wax on the structure. The sensitivities provided by the accelerometer's manufacturer were accepted as valid.

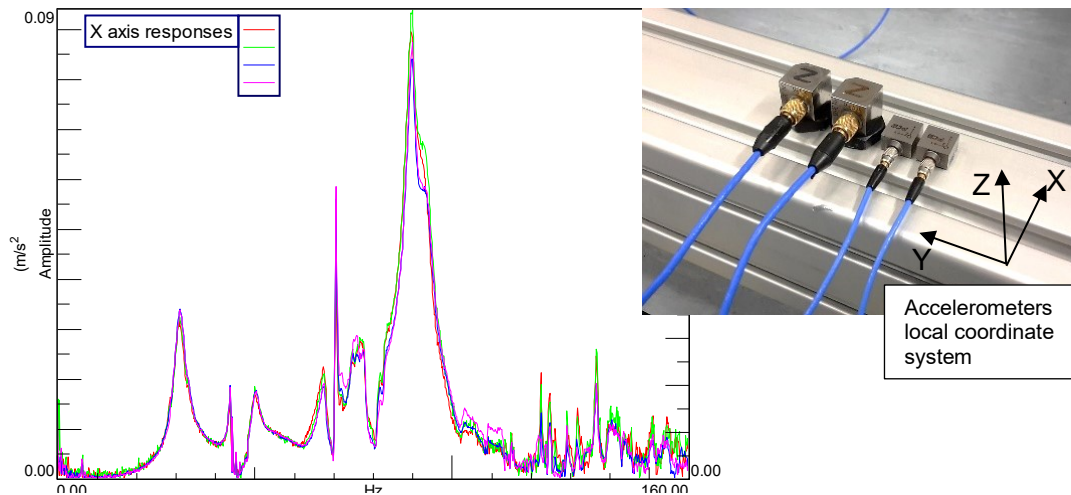


Figure 29. Qualitative comparison of the FRF of the four accelerometers in their X axis as a verification procedure.

5.1.2 Structure Preparation

Ideally in a modal test, a freely suspended condition of the test object is desired but there are many cases where this is practically impossible e.g. large civil structures. A freely supported test piece may also not be always preferred. For example when the regular operation condition of the object tested differs largely from a freely supported one [42]. For these reasons the OTS was tested in a regular operation condition, supported on the ground with the levelling feet.

Prior to the start of the experimental work, a complete scrutiny of the structure was carried out with the aim of finding loose screws. This would ensure an optimum and homogeneous condition of the tower. Indeed, a set of ten screws were found to be inadequately screwed in.

5.2 Test Planning

The test was planned taking into account the FEA results of the model. From those results, the frequency bandwidth of the test as well as preferred sensor and excitation locations were determined.

The impact locations were chosen to be on the upper platen in order to excite easily the majority of the modes. The platen, as a main connector element spreads the impact energy on the main four vertical aluminium extruded

profiles. Two orthogonal directions in the X and Y global axis of the OTS were chosen, crossing the centre of the tower.

Twenty-four sensor location were defined, which results in seventy-two responses (triaxial accelerometers). They were principally placed on the four vertical aluminium extruded profiles, following the different stories of the tower. Also in the middle of the upper and lower platens, in order to record the platen deflections.

Then the geometry of the OTS was defined on the acquisition software, LMS Test.Lab. Figure 30 show the geometry defined in LMS Test.Lab and the sensor locations. The red arrows represent the excitation directions on the upper platen.

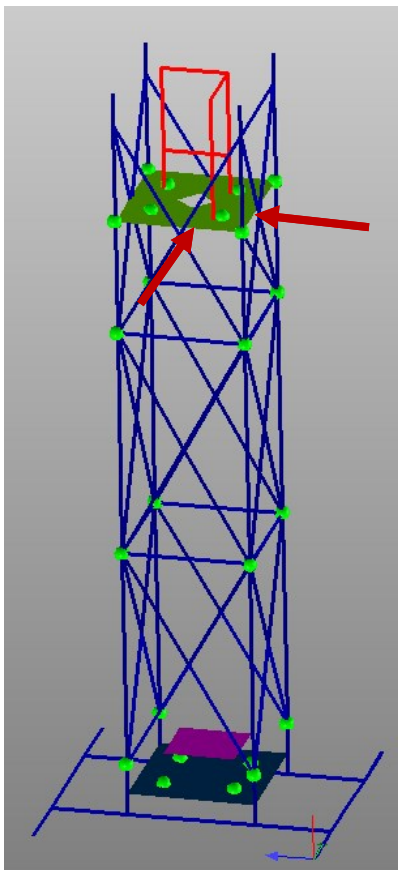


Figure 30. Accelerometers locations (green dots) and impact directions (red arrows) on the LMS Test.Lab geometry definition.

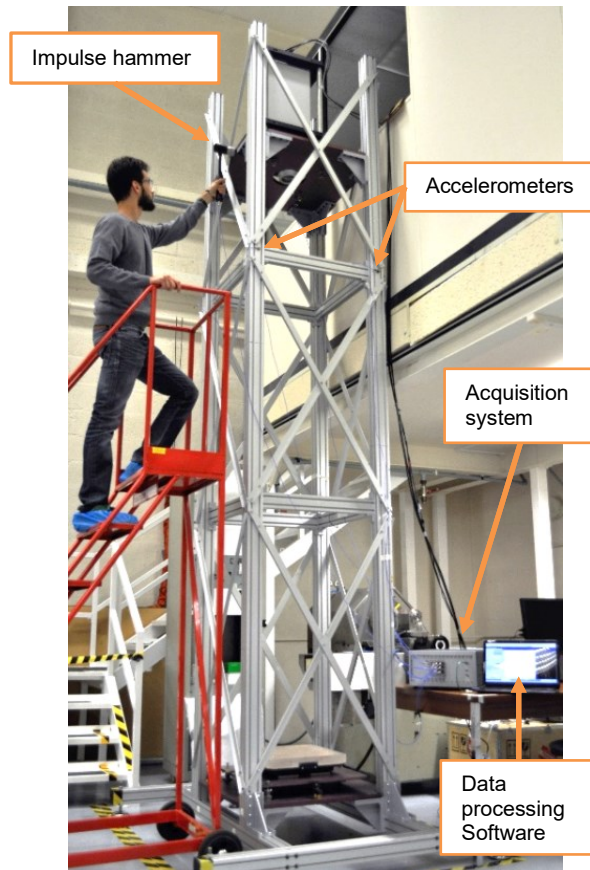


Figure 31. Experimental Setup with equipment identified.

5.3 Experimental Setup

Only four accelerometers were available so the tests were carried out in different runs. The positions of the sensors were changed both in each run and defining the new position and orientation on the data acquisition software. The data of five impacts were averaged for each configuration.

All the acquisitions were made at a sampling frequency of the ADC of 360 Hz (above the required Nyquist frequency for the frequency range in study up to 100 Hz). The acquisition system used for the experimental setup provided a minimum resolution of 0.15 Hz. that acquisition resolution was considered acceptable. Figure 31 shows a typical set up.

5.3.1 Acquisition procedure

The acquisition procedure could be summarized as following [43]. First, an impact signal (input) is provided using the impulse hammer onto a key location and direction. The accelerometers set at the predefined locations (Figure 30) convert the vibration into an analogue signal (responses). Both the input and response signals were acquired using the acquisition system. The system filtered and digitized the analogue signals (ADC converter). When necessary, a weighting function (window) was applied to the signal in order to enhance the periodicity of the signal. The periodicity of the signal is necessary for computing the Fast Fourier Transformation. Then the average of different runs is computed. Finally, the frequency response functions (FRF) between the input and each response point were obtained. Each trial produced a set of FRF that are stored as a matrix of measurement.

5.4 Modal Parameter Estimation

Once all the experimental data was acquired, it formed a matrix of FRF functions with a dimension of 72 responses x 2 inputs (excitations).

Then a modal parameter estimation (MPE) method was used to extract the natural frequencies and damping. These methods are based on curve fitting

algorithms in order to find stable real poles, which are the physical vibration modes of the studied structure.

The PolyMAX, a polyreference least-squares complex frequency-domain method, was used for their clarity in poles identification [44]. First, the stabilization diagram for the bandwidth between 0 and 100 Hz. The clearly stable real poles were selected. Figure 32 below show the stabilization diagram.

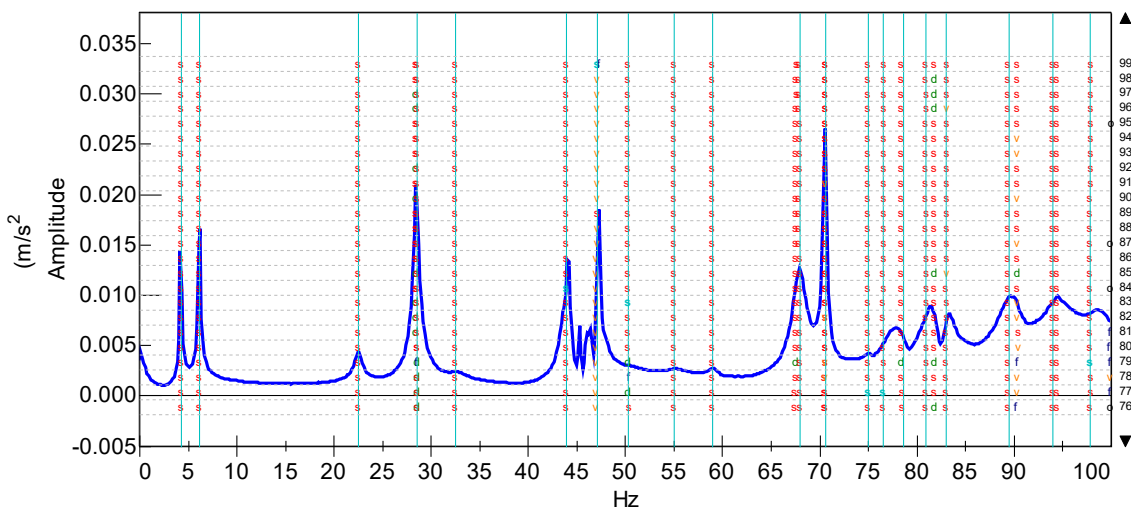


Figure 32. Stabilization chart with stable real poles selected.

Only the clearly identified modes were selected in the 40-50 Hz bandwidth. This choice supported by the FEA results. Indeed, it was determined that many local modes existed in this bandwidth.

The Auto-MAC was used as quality tool, to check that the modes selected were independent and well defined. The modal assurance criterion (MAC) [36], as defined on the literature review, is a mathematical tool used to determine the grade of correlation between two vectors of the same dimension, in this case mode shapes.

Figure 33 show the Auto-MAC matrix of the modes selected on the stabilization diagram (Figure 32). Some modes seemed to be highly coupled, such modes 6 & 7, 13 & 14, and 15 & 16. This high correlation between them could indicate that they were actually the same mode or that there was no enough data and spatial aliasing was taking place (different sensor locations would be needed).

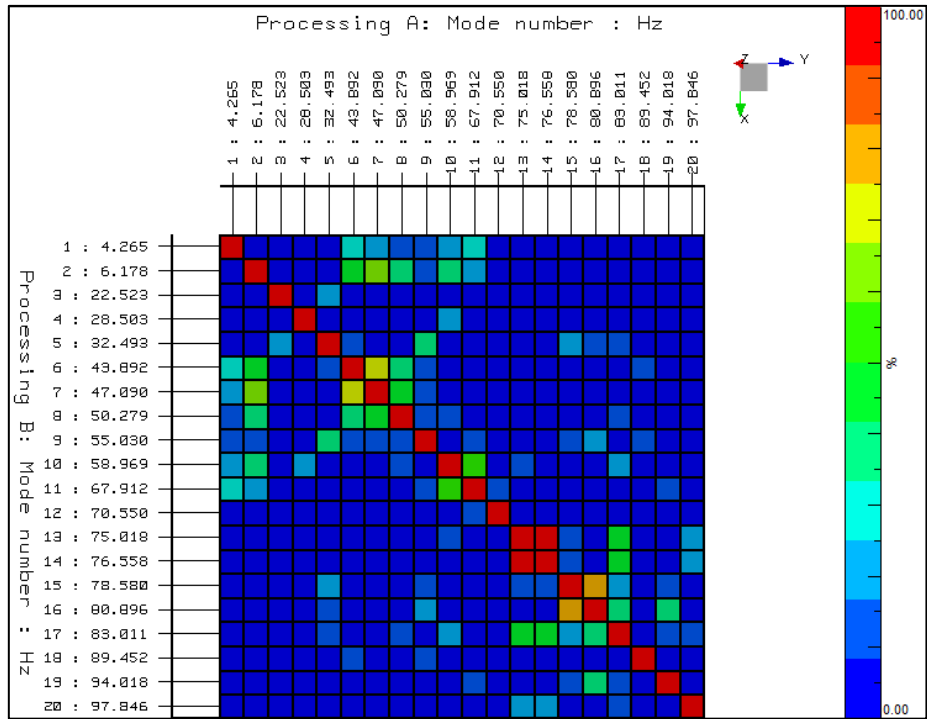


Figure 33. Auto-MAC matrix of the first set extracted.

In order to verify the modes selected, their graphical animations were checked and compared together.

Mode 7, 13 and 15 were excluded from the analysis; for reasons of similarity with other modes (modes 13 and 15), or for the lack of data to represent them properly (mode 7, a local mode).

Finally, the Auto-MAC matrix was computed with the new set of modes, which showed proper identification of all of them (Figure 34). The MAC values of correlation between modes remained below 50%.

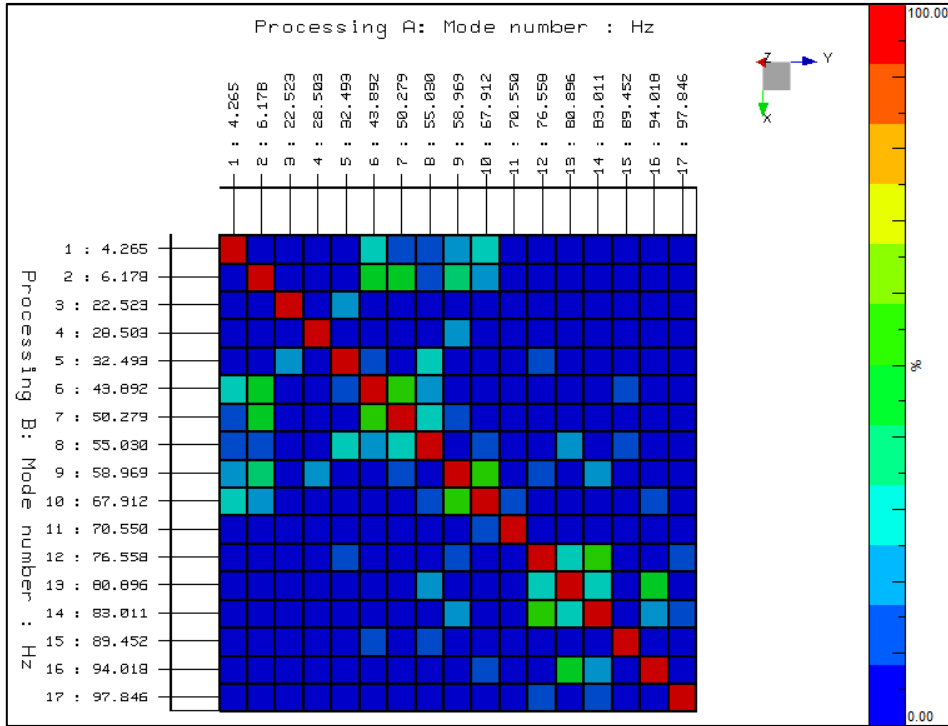


Figure 34. Auto-MAC matrix of the final set of modes.

Finally, the list of the modal parameters extracted from the Experimental Modal Analysis is listed in Table 3 below:

Table 3. Modal parameters estimated from the EMA.

	<i>Frequency. f [Hz]</i>	<i>Damping. ξ [%]</i>
Mode 1	4.26	0.57
Mode 2	6.18	0.55
Mode 3	22.52	1.18
Mode 4	28.50	0.73
Mode 5	32.49	2.60
Mode 6	43.89	0.73
Mode 7	50.28	1.27
Mode 8	55.03	2.03
Mode 9	58.97	0.96
Mode 10	67.91	0.99
Mode 11	70.55	0.17
Mode 12	76.56	0.78
Mode 13	80.89	1.28
Mode 14	83.01	0.44
Mode 15	89.45	1.28
Mode 16	94.01	1.25
Mode 17	97.85	1.25

At this point the experimental modal parameters -frequencies, damping and modes shape- were obtained. As a summary, the graphical representation of the modes obtained experimentally can be found on the Appendix B.

The graphical visualization aided the correlation and also the identification of discrepancy sources between the model and the real structure.

The mode 11 of the measured set revealed one source of discrepancy. This mode, at 70.55 Hz, shows an angular deformation of the square storeys of the tower, inducing a vibration mode (see Figure 35). Moreover, this mode showed a large amplitude on the FRF sum function of the stabilization chart (Figure 32). This mode did not appear on the FEA simulation since the joints between the square storeys extruded profiles were simulated as rigid.

A solution to the angular deformation of the square storeys was proposed, and it is detailed in the recommendations and further work chapter.

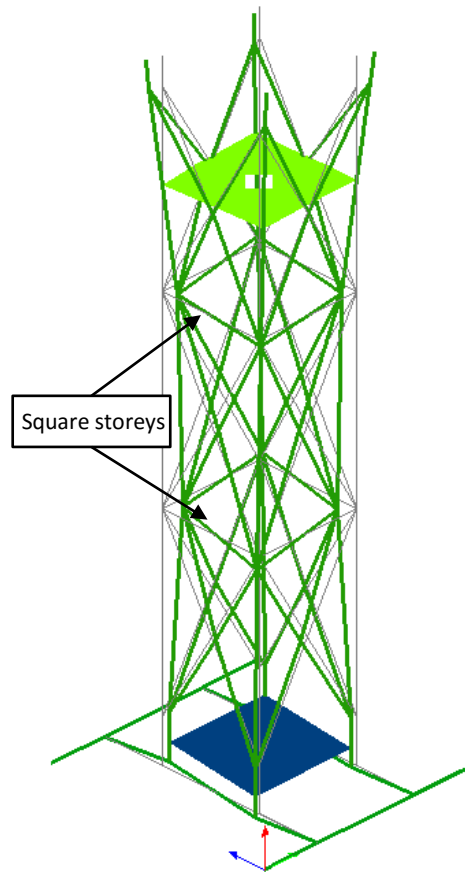


Figure 35. Mode shape at 70.6 Hz, mode 11 of the measured set. Note angular distortion of the square storeys of the tower.

6 RESULTS CORRELATION

The correlation between the results obtained through both the finite element analysis and the experimental analysis was carried out. This section details the analysis.

A first comparison between the graphical animations of the modes brought the correlation of the low frequency modes (1st to 4th). FEA and experimental results were correlated through frequency and mode shape. At higher frequencies, the mode shapes were more complex and a direct graphical identification was not straightforward. However, the modes were paired in frequency. Some modes remained unpaired. Figure 36 presents the correlation of natural frequencies.

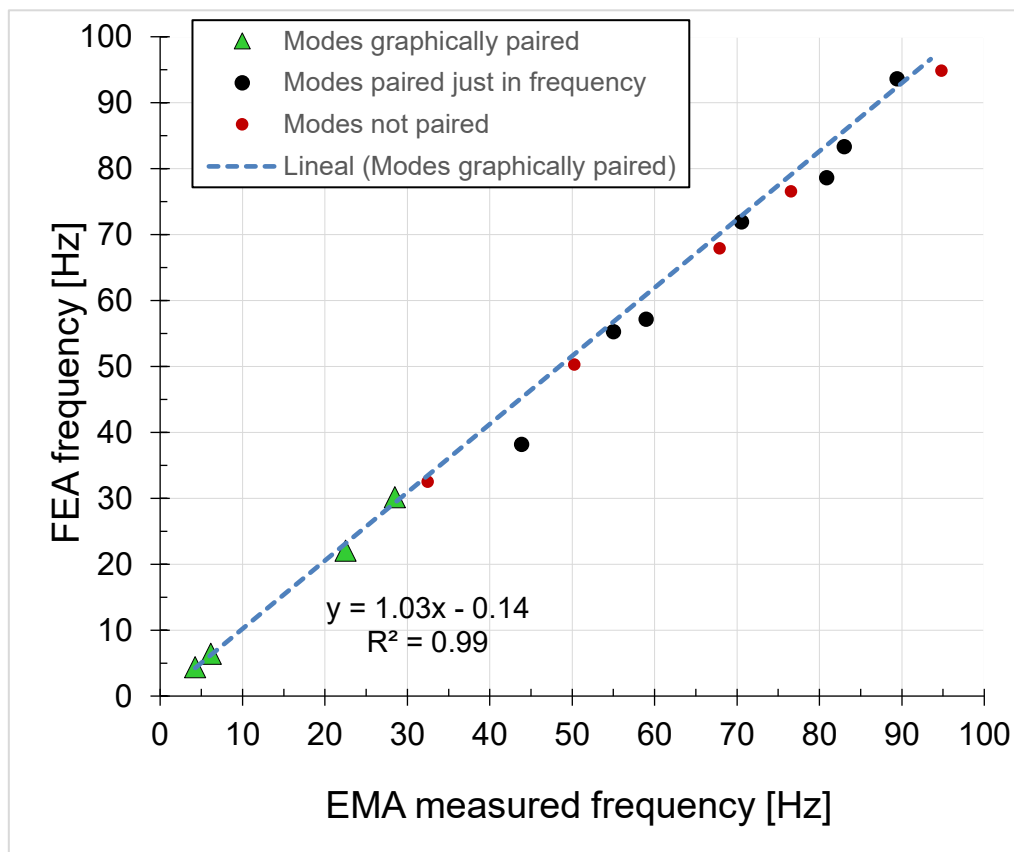


Figure 36. Measured and predicted natural frequencies.

A trend line was calculated just for the graphically paired modes, and it was then extrapolated. The other frequencies fell down near the trend line which gave confidence on the rest of results' validity.

The discrepancies on the frequency values were computed. Although, this method did not guarantee the correct mode pairing, it gave a quantitative evaluation of the correlation between the best fit frequencies. Table 4 shows both set of frequencies and their discrepancy on the natural frequency.

Table 4. Correlation in Frequency summary

	<i>Measured freq. [Hz]</i>	<i>FEA freq. [Hz]</i>	<i>Discrepancy in Frequency</i>
<i>Mode 1</i>	4.26	4.37	2.52%
<i>Mode 2</i>	6.18	6.43	3.89%
<i>Mode 3</i>	22.52	22.06	2.09%
<i>Mode 4</i>	28.50	30.16	5.50%
<i>Mode 5</i>	32.49	-	-
<i>Mode 6</i>	43.89	38.18	14.96%
<i>Mode 7</i>	50.28	-	-
<i>Mode 8</i>	55.03	55.28	0.45%
<i>Mode 9</i>	58.97	57.16	3.17%
<i>Mode 10</i>	67.91	-	-
<i>Mode 11</i>	70.55	71.92	1.90%
<i>Mode 12</i>	76.56	-	-
<i>Mode 13</i>	80.89	78.62	2.89%
<i>Mode 14</i>	83.01	83.34	0.40%
<i>Mode 15</i>	89.45	93.65	4.48%
<i>Mode 16</i>	94.01	-	-
<i>Mode 17</i>	97.85	109.38	10.54%

A successful correlation was achieved at low frequency modes, where the discrepancies were below 5% between the finite element model and the tested structure. Furthermore, the mode shapes were graphically paired which validated the correlation, see Figure 37.

Acceptable discrepancy values may depend on various aspects e.g. ambition and time scale of the study. In this case 5% is considered more than acceptable. Related literature on the field of model updating situates these values normally below 10% [45]–[47].

On higher frequencies, discrepancies were better than 15% and with a trend following the fully correlated modes (Figure 36). Nevertheless, a full correlation

cannot be concluded. A full graphical validation was not possible due to complex mode shapes and probably spatial aliasing on the experimental data (not enough sensing points).

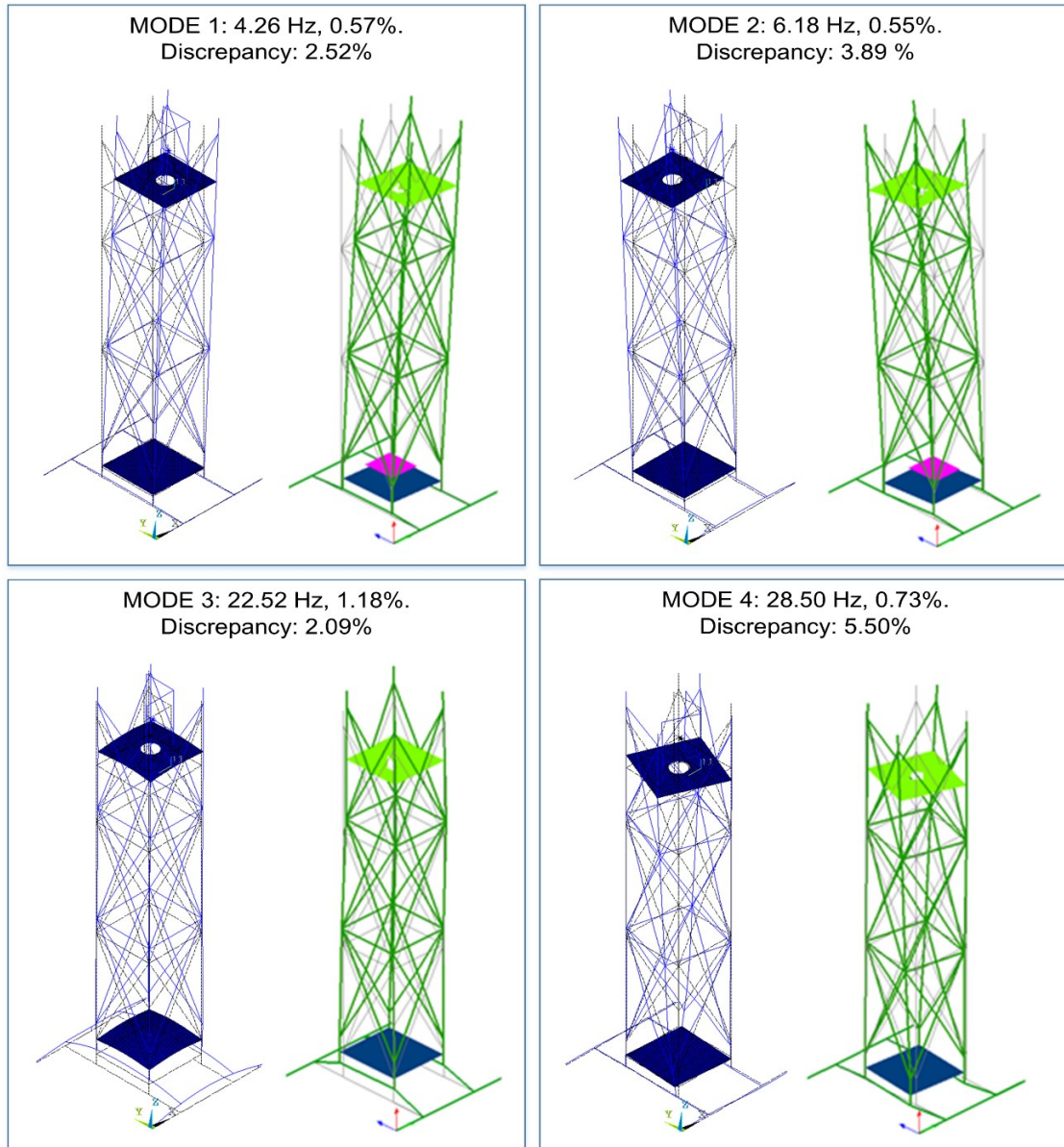


Figure 37. Graphically paired modes. Frequency, damping and discrepancy between the model (left side) and the experimental results (right side).

With the review of the results, the FE model was successfully validated up to 30 Hz. Further work would be needed to pair and correlate mathematically (with the MAC) the identified modes shape vectors at higher frequencies. This will enable the full validation of the model for a 0-100 Hz bandwidth.

7 TRANSMISSIBILITY STUDY

At this point of the project, the modal parameters of the structure were obtained and the finite element model was validated. This was the first and necessary step on the vibrational characterisation of the Optical Test System, and the principal aim of this thesis.

Even though results mentioned previously are highly valuable, they did not highlight the modes that might have a more adverse effect on the measurement capability of the OTS. In an attempt to apply the knowledge acquired practically, a step further was pursued and a new experimental set up was defined.

The OTS was assumed to work between two points of interest, the interferometer and the test piece. The ideal situation to reach the best measurement performance would be that the straight line between these points remains static i.e. no relative movement exists between the points of interest. It could be that even a mode induce sever vibrations on the OTS, the test piece and the interferometer move in 'phase' and no distortion of this ideal straight line occur. This was then the basic idea when planning a transmissibility study, a ratio to evaluate the relative vibration between these two points on the three axis, X, Y, and Z (Figure 38).

Transmissibility is a ratio that shows the relative vibration levels between two points (j, k) :

$$T_{jk}(\omega) = \frac{X_j \cdot e^{i\omega t}}{X_k \cdot e^{i\omega t}} \quad (7-1)$$

experimentally, it is a ratio between two transfer functions with a common excitation point (i):

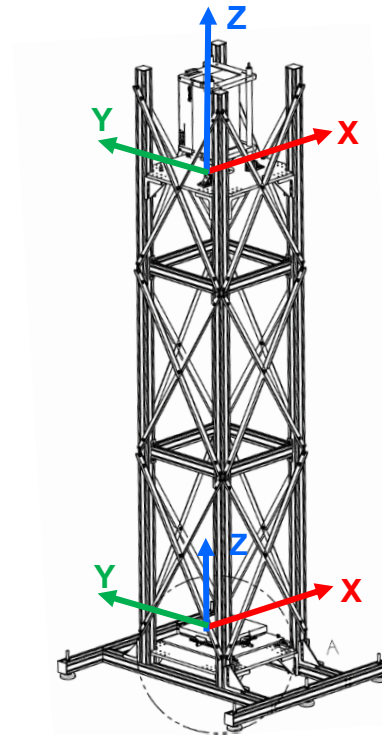


Figure 38. Cartesian coordinate systems for computing transmissibility functions.

$${}^i T_{jk}(\omega) = \frac{H_{ji}(\omega)}{H_{ki}(\omega)}, \quad (7-2)$$

and normally, transmissibility depends on the excitation point (i) or (q):

$${}^i T_{jk}(\omega) \neq {}^q T_{jk}(\omega). \quad (7-3)$$

Nevertheless, near the resonance frequencies it is independent from the excitation point:

$${}^i T_{jk}(\omega) = \frac{H_{ji}(\omega)}{H_{ki}(\omega)} = \frac{\sum_r \frac{\phi_{jr} \phi_{ir}}{(\omega_r^2 - \omega^2)}}{\sum_r \frac{\phi_{kr} \phi_{ir}}{(\omega_r^2 - \omega^2)}} \quad (7-4)$$

$${}^i T_{jk}(\omega)_{\omega \rightarrow \omega_{resonance}} = \frac{\phi_{ji}}{\phi_{ki}}. \quad (7-5)$$

Transmissibility is useful when the structure is lightly damped, and only one mode exist near resonance [42], [48], [49]. The OTS fulfilled these conditions.

An experimental transmissibility study was planned to have an accelerometer on the centre of the test piece and another on the outer case of the interferometer (Figure 39). Their axis (X, Y and Z) were parallel between them in order to compute later the transmissibility functions on the different directions.

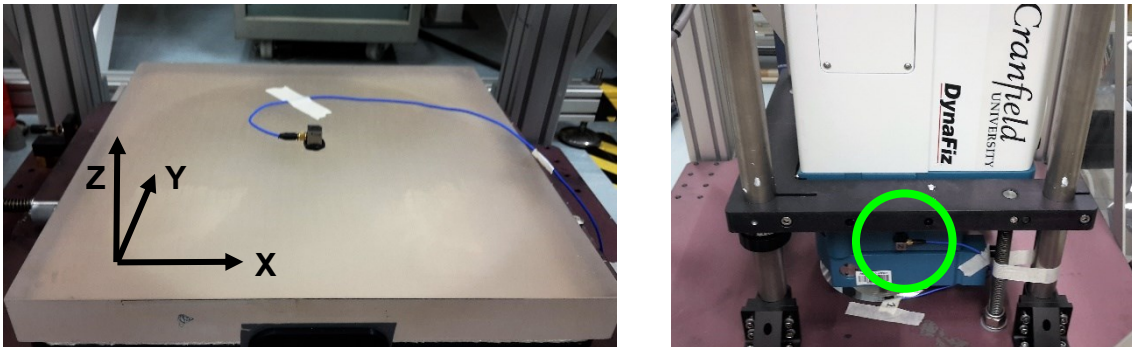


Figure 39. On the left, the accelerometer on the test piece centre. In black, the coordinate system for computing the transmissibility, X-Y is the test piece plane. On the right, the accelerometer on the interferometer's case.

From the theory (equation (7-5)), it was known that transmissibility function in a structure such the OTS would be independent from the excitation point. Nevertheless, the reality was that slightly changed functions were obtained when changing excitation positions. An average of different excitation points was then computed, and finally the transmissibility function of the two averages (from both upper and lower accelerometers) was calculated [48], [49]. Figure 40 shows the transmissibility function computed between the interferometer -upper accelerometer- and the test piece -lower accelerometer-. The Y axis show the decibels of the transmissibility ratio, on the X axis the frequency bandwidth. Superimposed with grey lines, there are the resonance frequencies of the modes extracted from the Experimental Modal Analysis (section 5.4).

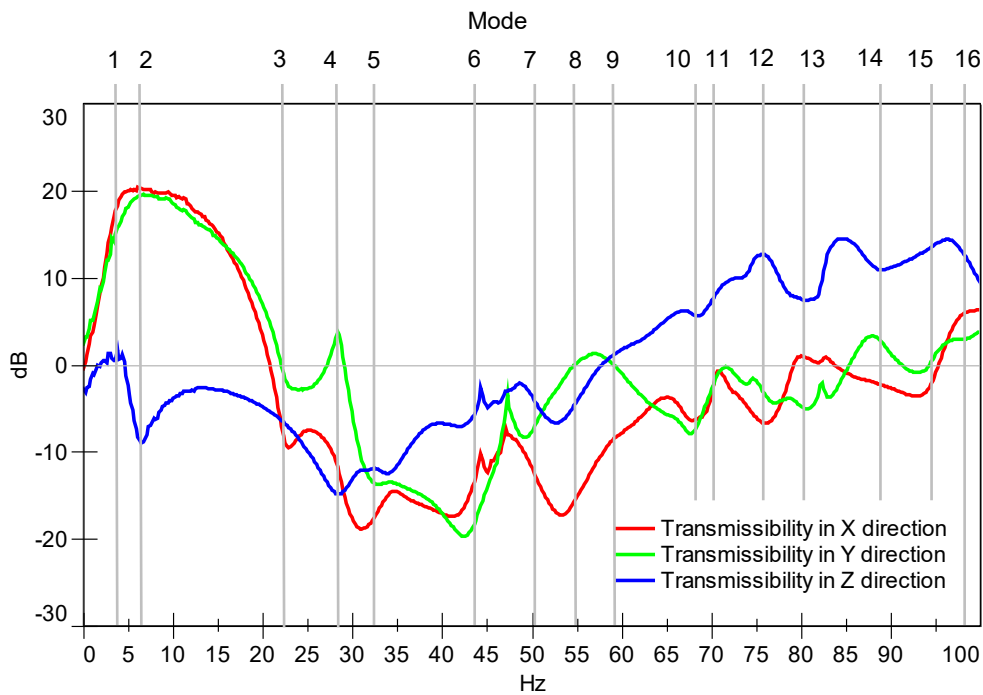


Figure 40. Transmissibility functions between the test piece and the interferometer.

Transmissibility on the test piece plane, i.e. X (red line) and Y (green line) directions, showed a big peak on a range between 0 and 20 Hz. This could be explained by the effect that the two first dominating modes have on the structure dynamics. These bending modes at 4.3 and 6.2 Hz cause a deflection of the whole tower; while the lower part of the tower is almost static, the upper part is oscillating, which could explain the high values on the transmissibility on

the test piece plane (X-Y directions). Moreover, despite of the shape of these modes, they dominate the structure dynamics being the easier modes to excite, which have an impact on the transmissibility ratio (bigger).

The fourth mode, the torsional mode, seems also to have a defined impact, at least on the Y direction. The differences between X and Y directions could be explained by the non-perfect central position of the accelerometer on the axis of rotation or an eccentricity on the torsional mode due to the non-symmetry of the structure. The accelerometer attached on the interferometer was not placed on the centre of rotation for practical reasons (see Figure 39). This hypothesis could be extrapolated on the other frequencies.

The transmissibility on the Z direction gained importance on the high frequency modes. No direct conclusions could be extracted from this fact, since the mode shapes at these frequencies were complex.

At this point, it is interesting to remember that the test piece was attached to the structure by a two stage positioning plate and an insulating foam. At the same time, the interferometer was secured on the upper platen by a pseudo kinematic support. These fastening supports introduce unknowns on the dynamics. These supports are likely to cause a degree of misinterpretations of the transmissibility function.

In order to strengthen the transmissibility study and to extrapolate the results on a possible scaling up the OTS structure, the same transmissibility function was computed between the upper and lower aluminium platens. This transmissibility study would enable to validate the results and to broaden our understanding. At the same time, the effect of the fastening supports could be understood when comparing the two set of transmissibility functions obtained.

Figure 41 shows the transmissibility functions between the upper and lower platens.

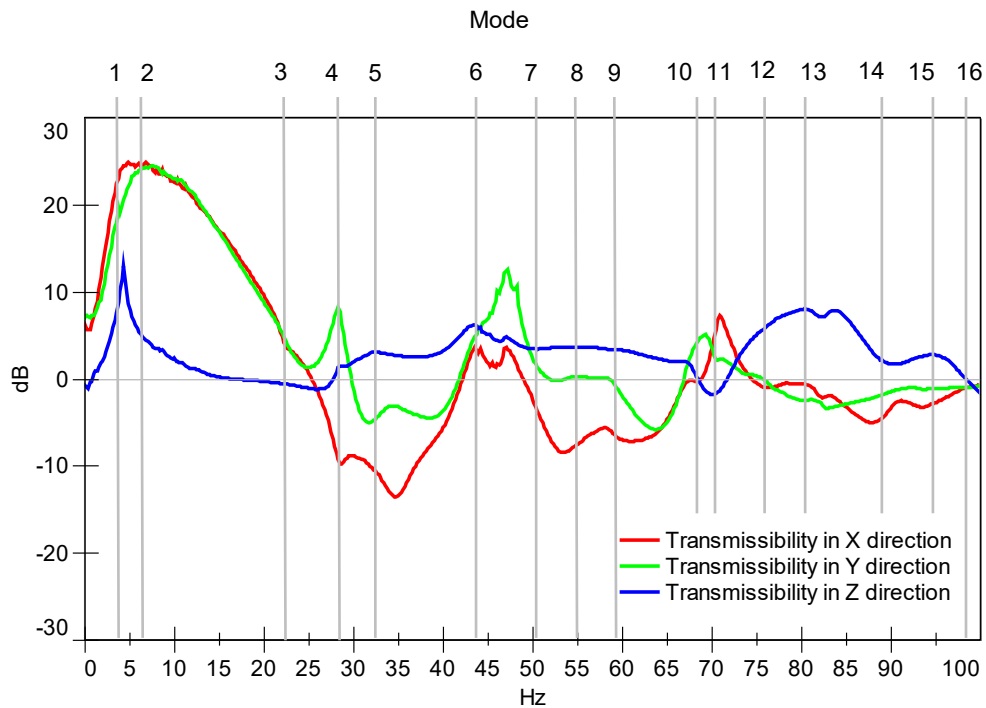


Figure 41. Transmissibility functions between platens.

The overall appearance of the functions resembles the ones on Figure 40. This preliminary assessment strengthens the validity of the previous study.

It is possible now to compare the transmissibility functions in each direction, between the function obtained through the test piece/interferometer and the two platens calculation. Further conclusions could be obtained.

Figure 42 and Figure 43 show the comparisons on the X and Y directions respectively. The functions between interferometer and test piece show lower values of transmissibility and a relatively similar function shape. A hypothesis that could explain the reduction on transmissibility is the damping effect of the insulating mat that sustains the test piece. It may also be an effect of the dynamics of the interferometer itself and its support structure.

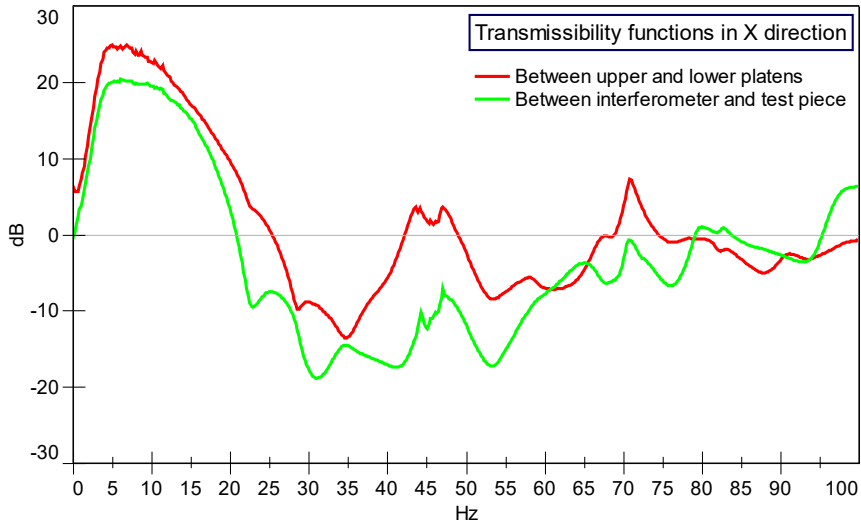


Figure 42. Comparison of the two transmissibility functions in X direction

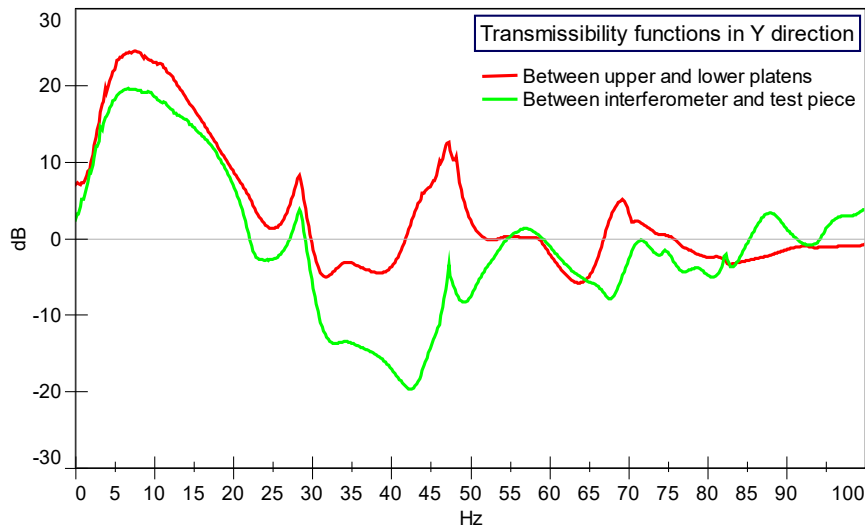


Figure 43. Comparison of the two transmissibility functions in Y direction.

In the Z direction, the resemblance between the functions is lower. Figure 44 shows the comparison of the transmissibility functions in the Z direction. Again, below 60 Hz, the function remains below the function computed between the platens, but the amplitude increases above that frequency. A hypothesis to explain the increase in amplitude at this bandwidth (60-100 Hz) could be the appearance of relevant local modes on the interferometer's support structure (Figure 4). Nevertheless, further study would be needed to clarify these effects.

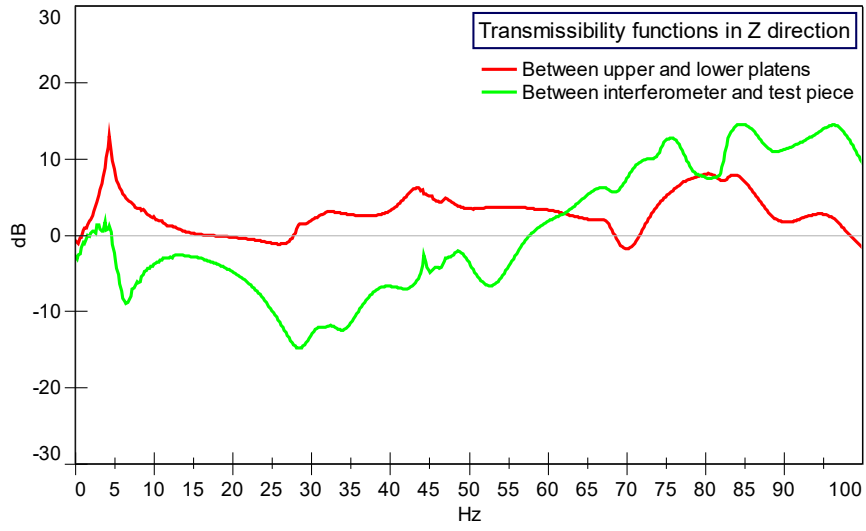


Figure 44. Comparison of the two transmissibility functions in Z direction.

8 RECOMMENDATIONS AND FURTHER WORK FOR ENHANCING THE OTS PERFORMANCE

From the knowledge acquired during the development of this project it was possible to recommend some ways for enhancing the OTS performance when scaling it up.

Different design strategies are presented and briefly discussed here. Their final applicability and further study are out of the scope of this thesis. They aim to be design directions for the scaling up process which could be used alone or as a combination of them.

8.1 Reinforcing the base structure

It has been seen that the low frequency modes are largely related with the base structure and the levelling feet of the OTS. Moreover, the transmissibility study (Chapter 7) showed that the 1st and 2nd modes may have the most detrimental effect on the measurement capability. Then increasing the natural frequencies of these modes will increase the robustness of the system.

8.1.1 Adding base supports

One of the main issues pinpointed is the length of the base profile that sustain the main vertical pillars. Their torsion facilitates the 1st mode or their vertical bending, the 3rd one (see Figure 37).

Adding levelling feet below the four main pillars will reduce the free length of the profile and it could stiffen the structure by the base on this critical element Figure 45.

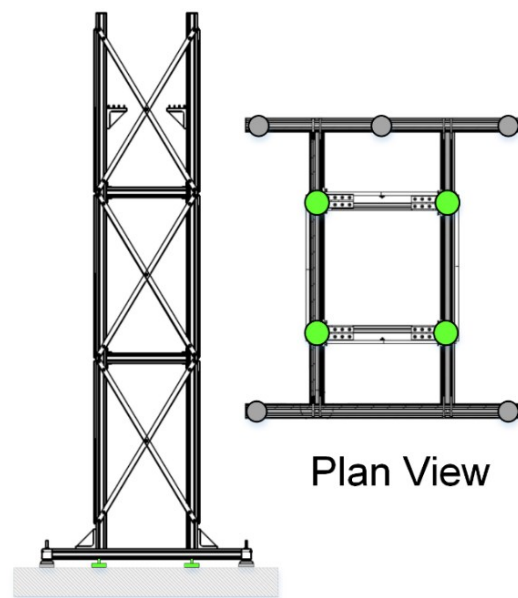


Figure 45. Base reinforcement schematic. In green, the added support below the main pillars of the OTS.

8.1.2 Reducing the free length of the tower

A more profound change on the design of the base structure is presented now. The main shape of the OTS, understood as tall and slender tower, could be simplified as a cantilever beam. The reduction of the free length of the beam increases the first natural frequencies. From the Euler-Bernoulli beam theory, the equation of the 1st natural frequency of a cantilever beam can be derivate as:

$$f_{n1} = \frac{1.875^2}{2\pi L^2} \sqrt{\frac{EI}{\rho A}} \quad (8-1)$$

Then it could be extrapolated that reducing the free length of the OTS will increase the natural frequencies of the first two bending modes –the ones affecting the most on the measurement capability– .

The recommendation, see Figure 46, is first to design the base structure surrounding the tower.

Then from this structure, reinforcement profiles could hold the tower from the sides, working as a buttress structures. The foot print of the tower remains small and modularity is not scarified.

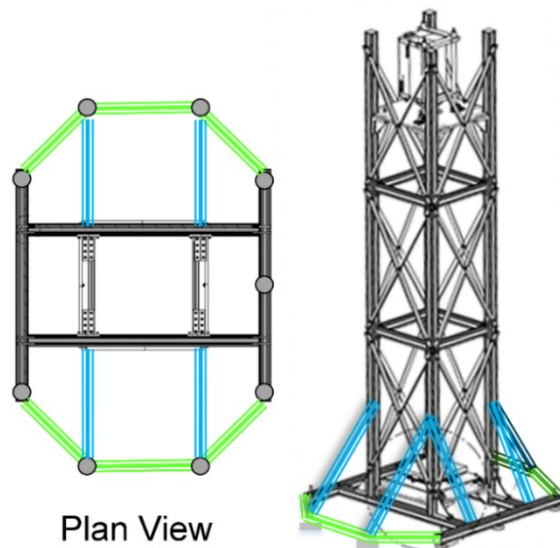


Figure 46. Surrounding base structure (in green) and buttress profiles (in blue).

8.2 Stiffening the square storeys

One weakness identified during the experimental work was the angular deformation of the square section of the OTS. This deflection induce the emergence of important vibration modes (end of Section 5.4). These modes could be mitigated by the reinforcement of the joints placing small blocking rods on the different storeys of the tower. A schematic is shown in Figure 47.

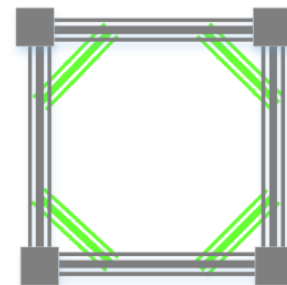


Figure 47. OTS square cross-section. In green, reinforcement rods.

8.3 Placing the structure on an insulating mat

The option of placing the structure, without any levelling feet, on a rubbery mat was first considered during the first design of the OTS.

This option needs to be studied carefully for proper selection of rubber mat parameters. This could lead to slightly stiffen the base structure which would be beneficial.

The main parameters that need to be tuned are the thickness of the mat, the elasticity modulus and the damping ratio of the material.

On the other hand, some issues need to be considered for this option. When placing the structure on a mat, a larger area is contacting on the base, which increase the transmission of energy from the ground to the tower. Moreover, the ‘free’ condition of the structure over a soft material may induce easily the appearance of rigid body modes.

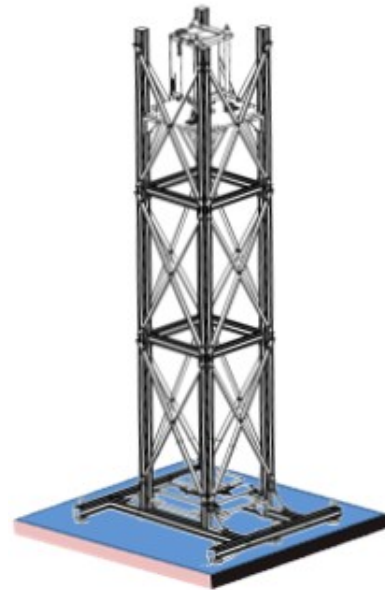


Figure 48. OTS without levelling feet over a rubber mat.

8.4 Structural material choice

During the project meetings with different stakeholders, it came out the discussion of building the OTS with steel instead of aluminium. The discussion came out because steel is cheaper and stiffer, but also heavier than aluminium.

In the vibrations field and for precision engineering applications what is significant is the specific stiffness (Young’s modulus divided by density) [50], which is very similar on both materials. They are listed on Table 5 below.

Table 5. Aluminium and steel mechanical properties and specific stiffness.

<i>Property</i>	<i>Units</i>	<i>Aluminium</i>	<i>Steel</i>
<i>Young’s Modulus, E</i>	<i>[GPa]</i>	75	210
<i>Density ρ</i>	<i>[kg/m³]</i>	2700	7800
<i>Specific Stiffness</i>	<i>[MNm/kg]</i>	27.8	26.9

Taking advantage of the OTS model, a simulation was done with the steel properties (without changing the structural profiles). The results were almost equal. The first natural frequency in aluminium is 4.37 Hz and in steel, 4.34 Hz.

Other parameters, like thermal ones, could be studied for other precision engineering applications. Nevertheless, on the OTS the thermal growth is considered to affect the structure at an insignificant rate compared with the acquisition speed of measurements.

Then in terms of material properties there would be no significant differences between a steel or aluminium structure. What needs to be studied further is the assembling methods and possible cost savings of the structure. Welding would be possible with steel, but then the modularity of the OTS is sacrificed.

9 CONCLUSIONS

The recently developed Optical Test System (OTS) of the Cranfield University Precision Engineering Institute is expected to become a high-performance and low-cost metrology station for large ultra-precise optical surfaces. The system will strengthen the metrology capability of the manufacturing chain for elements like the E-ELT segments, in growing demand worldwide.

As an underpinning of previous work on the novel system, this study enables a deeper understanding of the mechanical structure and the design parameters.

In this direction, the aim of this work was to explore the vibration characteristics of the OTS. To accomplish that aim, a finite element model of the OTS was created and a modal analysis performed. On the other hand, an experimental modal analysis was carried out.

The successful correlation between the experimental and numerical approaches enabled to validate the model. A 5% discrepancy on the natural frequencies was achieved for a frequency range between 0-30 Hz, where the mode shapes were graphically paired. Discrepancies lower than 15% were achieved for the frequency range between 30-100 Hz. The modal parameters of the structure – natural frequencies, damping and mode shapes– were obtained.

The first part of the project obtained a strong understanding of the vibration characteristics of the structure. In addition, the validated model provides a solid groundwork for further design and analysis of the OTS.

A step further was then pursued in order to clarify how the vibration characteristics could affect the interferometric metrology system performance. An experimental transmissibility study was carried out between the interferometer and the test piece.

The results revealed the effect of each vibration mode on the measurement capability of the OTS. It was determined that the first two bending modes (4.26 Hz and 6.18 Hz) are likely to present the most detrimental effects. The study set the basis for a further investigation on the interaction between the laser

interferometer's measurements and the vibration characteristics of the system. It also showed the damping effects of the fastening method of the test piece.

Finally, the knowledge acquired was transferred as suggestions for design improvements of the OTS. The base of the tower should be reinforced and design guidelines are provided. Moreover, the square storeys of the tower should be strengthen in order to mitigate the appearance of some of the modes. These are expected to be advantageous recommendations on the process of enhancing the measurement capability and scaling up the OTS in a near future.

REFERENCES

- [1] P. Shore, C. Cunningham, D. DeBra, C. Evans, J. Hough, R. Gilmozzi, H. Kunzmann, P. Morantz, and X. Tonnellier, "Precision engineering for astronomy and gravity science," *CIRP Ann. - Manuf. Technol.*, vol. 59, no. 2, pp. 694–716, Jan. 2010.
- [2] C. Cunningham, "Future technologies for optical and infrared telescopes and instruments," *Exp. Astron.*, vol. 26, no. 1–3, pp. 179–199, Aug. 2009.
- [3] R. Gilmozzi, "Science and technology drivers for future giant telescopes," in *Proceedings of SPIE - The International Society for Optical Engineering*, 2004, vol. 5489, no. PART 1, pp. 1–10.
- [4] M. Johns, "The Giant Magellan Telescope (GMT)," vol. 6267, p. 626729, 2006.
- [5] L. M. Stepp and S. E. Strom, "The Thirty-Meter Telescope project design and development phase," in *Proceedings of SPIE - The International Society for Optical Engineering*, 2004, vol. 5382, no. PART 1, pp. 67–75.
- [6] R. Gilmozzi and J. Spyromilio, "The European Extremely Large Telescope (E-ELT)," *The Messenger*, vol. 127, no. March, p. 11, 2007.
- [7] A. P. Russell, G. Monnet, A. Quirrenbach, R. Bacon, M. Redfern, T. Andersen, A. Ardeberg, E. Atad-Ettedgui, and T. G. Hawarden, "Instruments for a European Extremely Large Telescope: the challenges of designing instruments for 30- to 100-m telescopes," in *Proceedings of SPIE - The International Society for Optical Engineering*, 2004, vol. 5492, no. PART 3, pp. 1796–1809.
- [8] P. Shore, M. Castelli, P. Comley, R. Jourdain, J. Mitchell, P. Morantz, and X. Tonnellier, "UK developments towards rapid process chains for metre scale optics," in *Optics InfoBase Conference Papers*, 2012.
- [9] P. Comley, P. Morantz, P. Shore, and X. Tonnellier, "Grinding metre scale mirror segments for the E-ELT ground based telescope," *CIRP Ann. -*

- Manuf. Technol.*, vol. 60, no. 1, pp. 379–382, 2011.
- [10] R. Jourdain, M. Castelli, P. Shore, P. Sommer, and D. Proscia, “Reactive atom plasma (RAP) figuring machine for meter class optical surfaces,” *Prod. Eng.*, vol. 7, no. 6, pp. 665–673, Nov. 2013.
- [11] P. Shore, P. Morantz, X. Luo, X. Tonnellier, R. Collins, A. Roberts, R. May-Miller, and R. Read, “Big OptiX ultra precision grinding/measuring system,” *Proc. SPIE*, vol. 5965, pp. 241–248, 2005.
- [12] C. Fanara, P. Shore, J. R. Nicholls, N. Lyford, J. Kelley, J. Carr, and P. Sommer, “A New Reactive Atom Plasma Technology (RAPT) for Precision Machining: the Etching of ULE® Surfaces,” *Adv. Eng. Mater.*, vol. 8, no. 10, pp. 933–939, Oct. 2006.
- [13] J. W. Carr, “Apparatus and method for atmospheric pressure reactive atom plasma processing for shaping of damage free surfaces,” WO 2002060828 A2, 2002.
- [14] R. Jourdain, P. Morantz, and P. Shore, “Design and characterization of an optical test system for metre-scale optics,” *Opt. Express (to be Submitt.*, 2013.
- [15] D. Malacara, *Optical Shop Testing: Third Edition*. wiley, 2006.
- [16] L. Deck, “Vibration-resistant phase-shifting interferometry,” vol. 35, no. 34, pp. 6655–6662, 1996.
- [17] P. L. Wizinowich, “Phase shifting interferometry in the presence of vibration: a new algorithm and system.,” *Appl. Opt.*, vol. 29, no. 22, pp. 3271–3279, 1990.
- [18] C. Zhao and J. H. Burge, “Vibration-compensated interferometer for surface metrology.,” *Appl. Opt.*, vol. 40, no. 34, pp. 6215–6222, 2001.
- [19] L. L. Deck, “Suppressing phase errors from vibration in phase-shifting interferometry.,” *Appl. Opt.*, vol. 48, no. 20, pp. 3948–3960, 2009.
- [20] P. J. de Groot, “Vibration in phase-shifting interferometry,” *J. Opt. Soc.*

- Am. A Opt. Image Sci. Vis.*, vol. 12, no. 2, pp. 354–365, 1995.
- [21] P. J. de Groot and L. L. Deck, “Numerical simulations of vibration in phase-shifting interferometry,” *Appl. Opt.*, vol. 35, no. 13, pp. 2172–8, 1996.
- [22] D. M. Sykora and P. de Groot, “Instantaneous Interferometry: Another View,” in *International Optical Design Conference and Optical Fabrication and Testing*, 2010, p. OMA1.
- [23] D. C. Williams, N. S. Nassar, J. E. Banyard, and M. S. Virdee, “Digital phase-step interferometry: a simplified approach,” *Opt. Laser Technol.*, vol. 23, no. 3, pp. 147–150, 1991.
- [24] J. L. McLaughlin and B. A. Horwitz, “Real-time snapshot interferometer,” in *SPIE Vol. 680*, 1986, pp. 35–43.
- [25] P. F. Forman, “The Zygo inteferometer system,” *Interferometry*, vol. 0192, no. Aug, pp. 41–48, 1979.
- [26] D. M. Sykora and P. de Groot, “Instantaneous measurement Fizeau interferometer with high spatial resolution,” in *Proceedings of SPIE*, 2011, vol. 8126, p. 812610.
- [27] D. M. Sykora and M. L. Holmes, “Dynamic measurements using a Fizeau interferometer,” in *Proceedings of SPIE*, 2011, vol. 8082, p. 80821R.
- [28] J. H. Burge, “Advanced techniques for measuring primary mirrors for astronomical telescopes,” PhD thesis, The University of Arizona, 1993.
- [29] M. Cayrel, “Completion of VLT and GEMINI primary mirrors at REOSC,” in *Proceedings of SPIE - The International Society for Optical Engineering*, 2000, vol. 4003, pp. 14–23.
- [30] J. H. Burge, L. B. Kot, H. M. Martin, R. Zehnder, and C. Zhao, “Design and analysis for interferometric measurements of the GMT primary mirror segments,” in *Proceedings of SPIE - The International Society for Optical Engineering*, 2006, vol. 6273 I, p. 62730M.

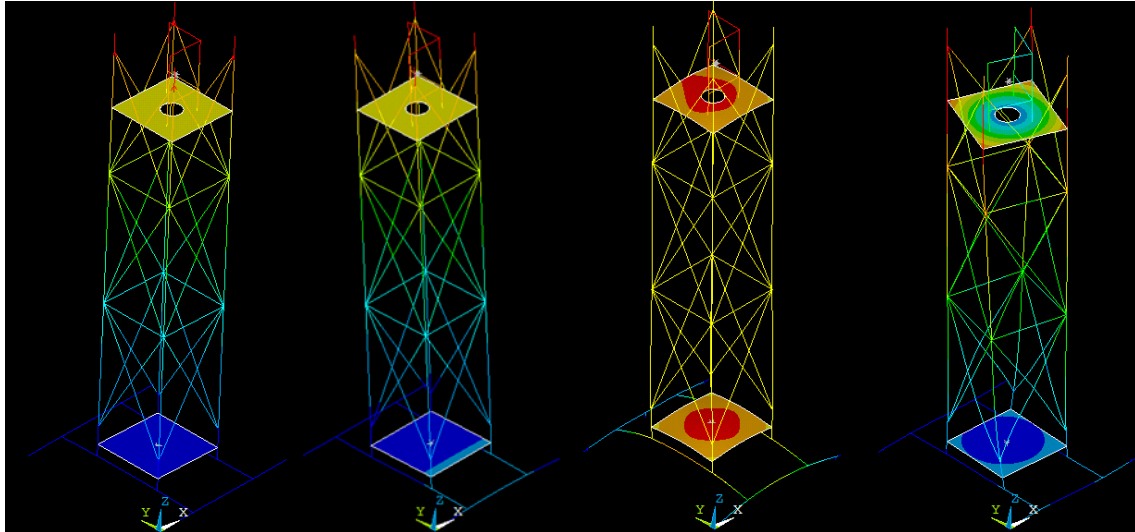
- [31] G. C. Cole, J. H. Burge, and L. R. Dettmann, "Vibration stabilization of a phase-shifting interferometer for large optics," vol. 3134, pp. 438–446, 1997.
- [32] M. Petyt and P. Gardonio, "Finite element techniques for structural vibration," in *Advanced Applications in Acoustics, Noise and Vibration*, F. Fahy and J. Walker, Eds. London: Taylor & Francis, 2004, pp. 448–489.
- [33] R. G. Grimes, J. G. Lewis, and H. D. Simon, "A Shifted Block Lanczos Algorithm for Solving Sparse Symmetric Generalized Eigenproblems," *SIAM J. Matrix Anal. Appl.*, vol. 15, no. 1, pp. 228–272, Nov. 1996.
- [34] C. Rajakumar and C. Rogers, "The Lanczos Algorithm Applied to Unsymmetric Generalized Eigenvalue Problems," *Int. J. Numer. Method Eng.*, vol. 32, pp. 1009–1026, 1991.
- [35] ANSYS®, "Theory Reference," in *Mechanical APDL 16.2*.
- [36] R. J. Allemang, "The modal assurance criterion - Twenty years of use and abuse," *Sound Vib.*, vol. 37, no. 8, pp. 14–21, 2003.
- [37] F. Wang, Z. Su, Q. Li, and J. Yang, "Response Analysis of Cathead Transmission Tower Seismic Performance Based on Open SEES," in *2014 Fifth International Conference on Intelligent Systems Design and Engineering Applications*, 2014, pp. 893–896.
- [38] Liu Xiaofeng, "The study on modal analysis theory and measurement method for transmission towers," in *2011 Second International Conference on Mechanic Automation and Control Engineering*, 2011, pp. 1827–1831.
- [39] G. McClure and M. Lapointe, "Modeling the structural dynamic response of overhead transmission lines," *Comput. Struct.*, vol. 81, no. 8–11, pp. 825–834, 2003.
- [40] G. Chen, "FE model validation for structural dynamics," PhD thesis, University of London, 2001.

- [41] X. Chen, W. Wu, X. Fu, and Y. Xu, "Design and precision performance research of exact constraint support structure," 2010, vol. 7654, p. 76541K.
- [42] D. J. Ewins, *Modal Testing: Theory, Practice and Application*, 2nd ed. Research Studies Press LTD., 2000.
- [43] P. Avitabile, "Experimental Modal Analysis," *Sound Vib.*, no. January, pp. 1–11, 2002.
- [44] B. Peeters, H. Van Der Auweraer, P. Guillaume, and J. Leuridan, "The PolyMAX frequency-domain method: a new standard for modal parameter estimation?," *Shock Vib.*, vol. 11, pp. 395–409, 2004.
- [45] G. Boscato, S. Russo, R. Ceravolo, and L. Z. Fragonara, "Global sensitivity-based model updating for heritage structures," *Comput. Civ. Infrastruct. Eng.*, vol. 30, no. 8, pp. 620–635, 2015.
- [46] F. Shabbir and P. Omenzetter, "Model updating using genetic algorithms with sequential niche technique," *Eng. Struct.*, vol. 120, pp. 166–182, 2016.
- [47] M. I. Friswell and J. E. Mottershead, *Finite Element Model Updating in Structural Dynamics*. London: Kluwer Academic Publishers, 1995.
- [48] W. Liu and D. J. Ewins, "Transmissibility properties of MDOF systems," *Proc. Int. Modal Anal. Conf. - IMAC*, vol. 2, pp. 847–854, 1998.
- [49] N. M. M. MAIA, J. M. M. SILVA, and A. M. R. RIBEIRO, "the Transmissibility Concept in Multi-Degree-of-Freedom Systems," *Mech. Syst. Signal Process.*, vol. 15, no. 1, pp. 129–137, 2001.
- [50] D. G. Chetwynd, "Selection of structural materials for precision devices," *Precis. Eng.*, vol. 9, no. 1, pp. 3–6, 1987.

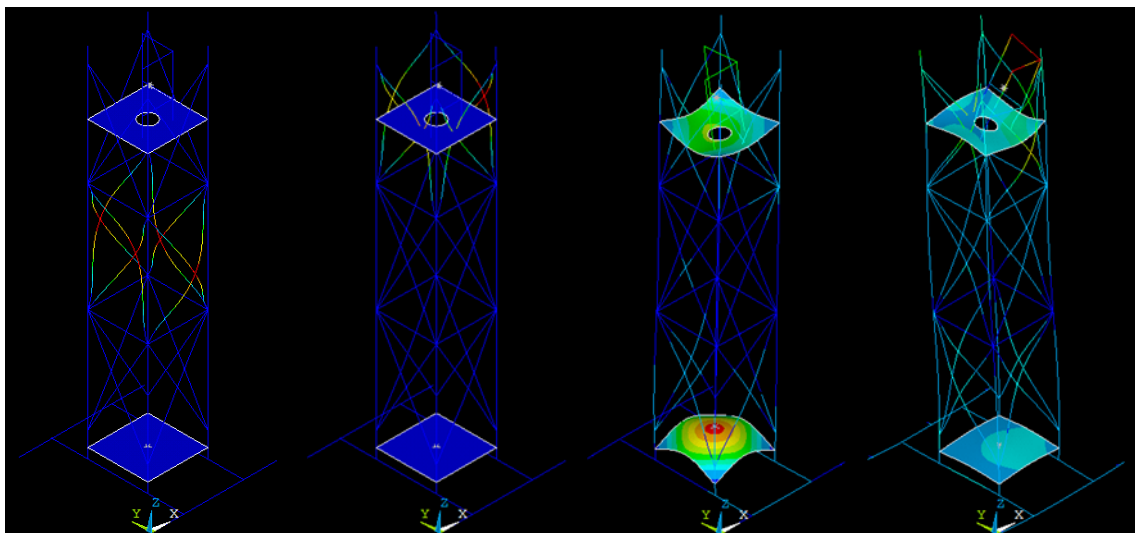
APPENDICES

Appendix A FEA Results

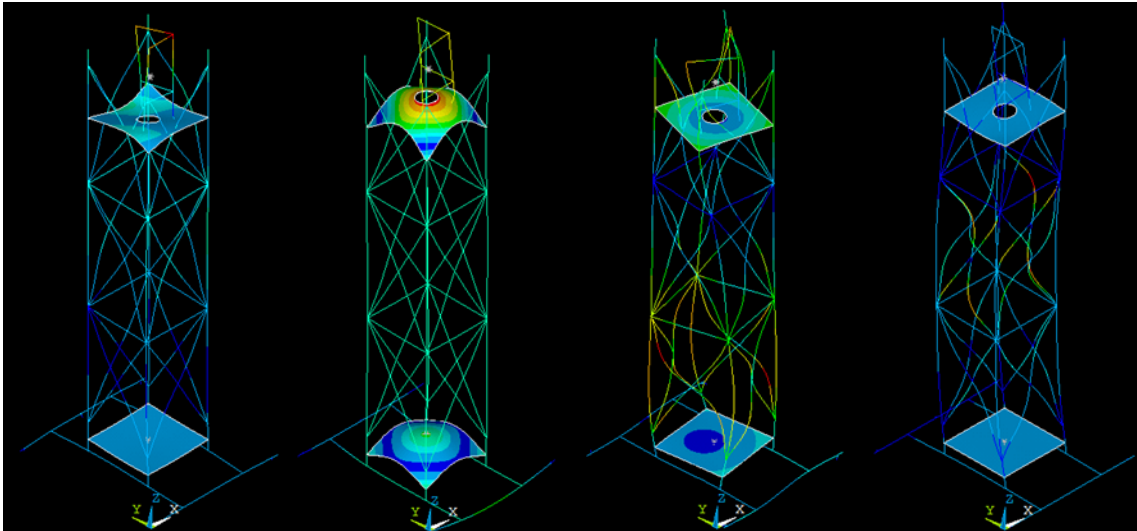
Results of the finite element analysis. Displacement vector sum and natural frequency, not to scale.



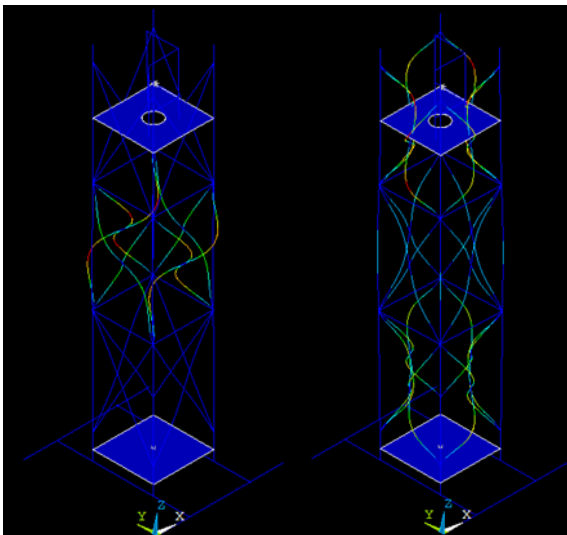
Mode 1. 4.37 Hz **Mode 2.** 6.43 Hz **Mode 3.** 22.06 Hz **Mode 4.** 30.16 Hz



Local Modes from Mode 5 (38.18 Hz) to Mode 18 (49.26 Hz). Pictures: on the left, Mode 7 (42.81 Hz); on the right, Mode 15 (46.49 Hz). **Mode 19.** 55.28 Hz **Mode 20.** 57.16 Hz



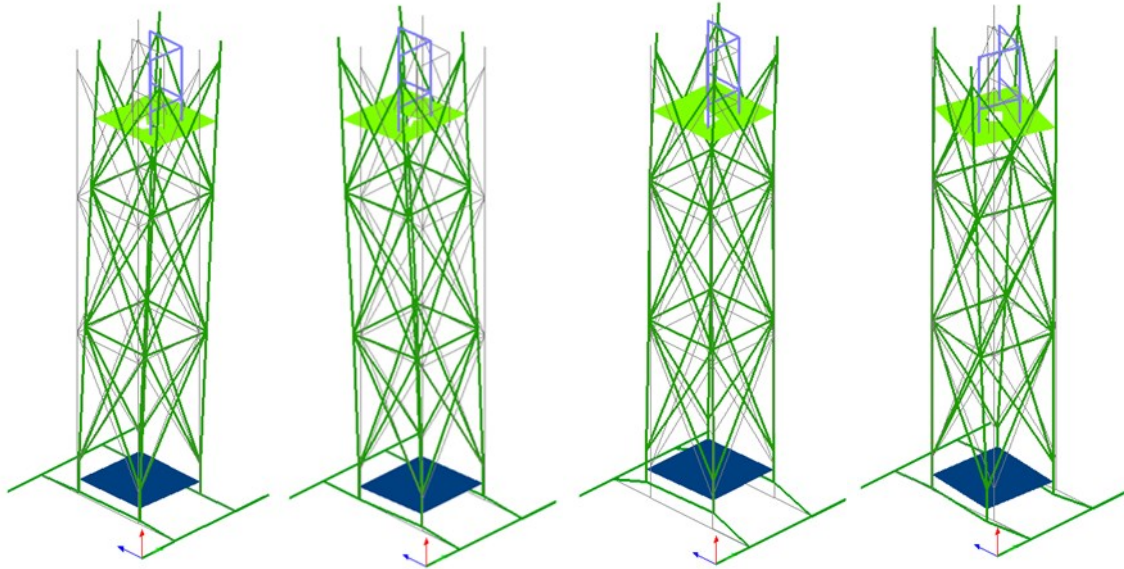
Mode 21. 71.92 Hz **Mode 22.** 78.62 Hz **Mode 23.** 83.34 Hz **Mode 24.** 93.66 Hz



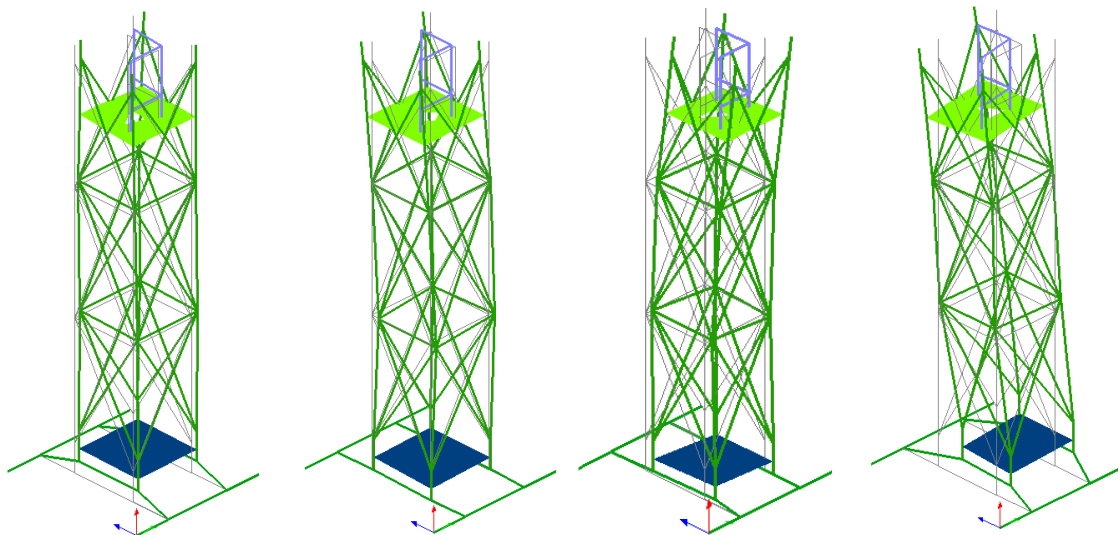
Local Modes from Mode 25 (95.33 Hz) to Mode 51 (115.85 Hz). Pictures: on the left, Mode 25; on the right, Mode 51.

Appendix B EMA results

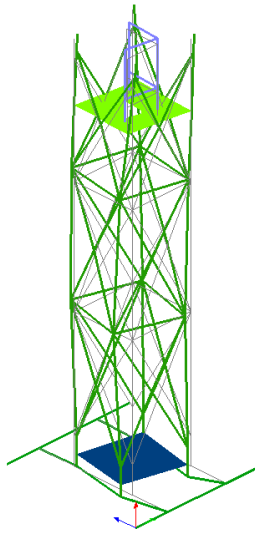
Experimentally identified modes. Expanded mode shape, natural frequency and damping ratio. Drawings not to scale.



Mode 1.	Mode 2.	Mode 3.	Mode 4.
4.26 Hz, 0.57%	6.18 Hz, 0.55%	22.52 Hz, 1.18%	28.50 Hz, 0.73%

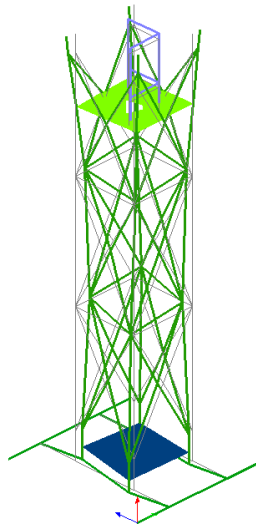


Mode 5.	Mode 6.	Mode 7.	Mode 8.
32.49 Hz, 2.60%	43.89 Hz, 0.73%	50.28 Hz, 1.27%	55.03 Hz, 2.08%



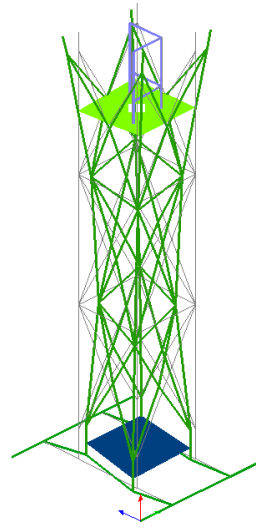
Mode 9.

58.97 Hz, 0.96%



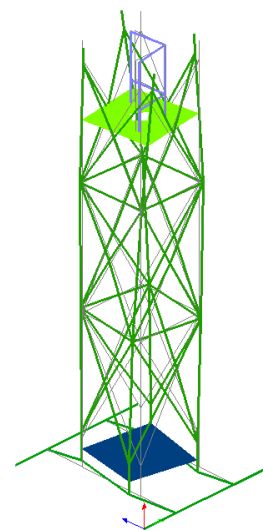
Mode 10.

67.91 Hz, 0.99%



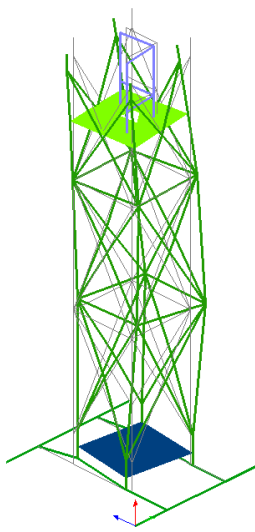
Mode 11.

70.55, 0.17% Hz



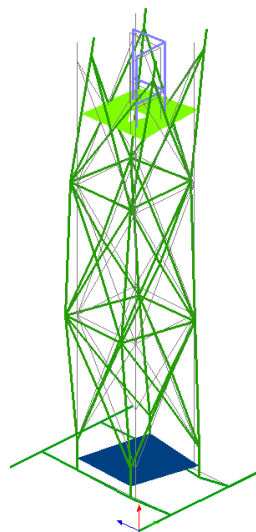
Mode 12.

76.56 Hz, 0.78%



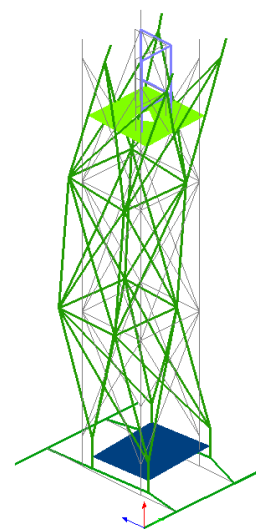
Mode 13.

80.89 Hz, 1.28%



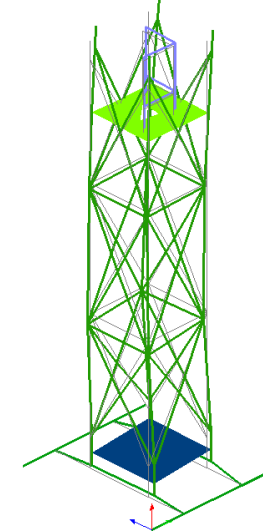
Mode 14.

83.01 Hz, 0.44%



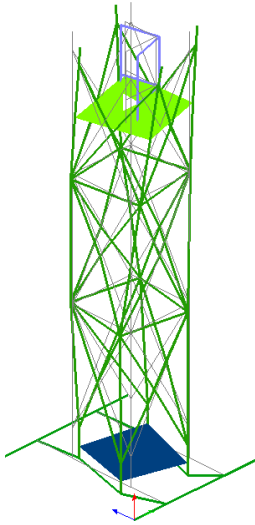
Mode 15.

89.45 Hz, 1.28%



Mode 16.

94.01 Hz, 1.25%



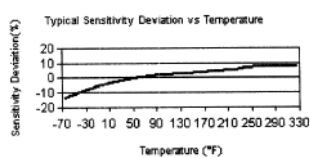
Mode 17.

97.85 Hz, 1.25%

Appendix C Equipment Data Sheets

Model Number 356A24	TRIAxIAL ICP® ACCELEROMETER		Revision: F ECN #: 42197
Performance	ENGLISH	SI	OPTIONAL VERSIONS
Sensitivity(± 1%)	10 mV/g	1.02 mV/(m/s ²)	Optional versions have identical specifications and accessories as listed for the standard model except where noted below. More than one option may be used.
Measurement Range	± 500 g pk	± 4905 m/s ² pk	HT - High temperature, extends normal operation temperatures
Frequency Range(± 5%)	1 to 6000 Hz	1 to 6000 Hz	Temperature Range(Operating)
Frequency Range(± 10%)	0.5 to 12,000 Hz	0.5 to 12,000 Hz	-65 to +325 °F
Resonant Frequency	≥ 45 kHz	≥ 45 kHz	-54 to +163 °C
Broadband Resolution(1 to 10,000 Hz)	0.004 g rms	0.04 m/s ² rms	J - Ground Isolated
Non-Linearity	≤ 1%	≤ 1%	Electrical Isolation(Base)
Transverse Sensitivity	≤ 5%	≤ 5%	10 ⁵ Ohm
Environmental			10 ⁵ Ohm
Overload Limit(Shock)	± 10,000 g pk	± 98,100 m/s ² pk	Size - Height x Length x Width
Temperature Range(Operating)	-65 to +250 °F	-54 to +121 °C	0.33 in x 0.47 in x 0.47 in
Temperature Response	See Graph	See Graph	8.3 mm x 12.0 mm x 12.0 mm
Electrical			Weight
Excitation Voltage	18 to 30 VDC	18 to 30 VDC	0.13 oz
Constant Current Excitation	2 to 20 mA	2 to 20 mA	3.7 gm
Output Impedance	≤ 200 Ohm	≤ 200 Ohm	
Output Bias Voltage	7 to 12 VDC	7 to 12 VDC	
Discharge Time Constant	1.0 to 3.5 sec	1.0 to 3.5 sec	
Settling Time(within 10% of bias)	<10 sec	<10 sec	
Spectral Noise(1 Hz)	900 µg/√Hz	8820 (µm/sec ²)/√Hz	NOTES:
Spectral Noise(10 Hz)	250 µg/√Hz	2450 (µm/sec ²)/√Hz	[1] Typical.
Spectral Noise(100 Hz)	100 µg/√Hz	981 (µm/sec ²)/√Hz	[2] 250° F to 325° F data valid with HT option only.
Spectral Noise(1 kHz)	50 µg/√Hz	490 (µm/sec ²)/√Hz	[3] Zero-based, least-squares, straight line method.
Physical			[4] See PCB Declaration of Conformance PS023 for details.
Sensing Element	Ceramic	Ceramic	
Sensing Geometry	Shear	Shear	
Housing Material	Titanium	Titanium	
Sealing	Hermetic	Hermetic	
Size (Height x Length x Width)	0.28 in x 0.47 in x 0.47 in	7.0 mm x 12.0 mm x 12.0 mm	
Weight(without cable)	0.11 oz	3.1 gm	
Electrical Connector	8-36 4-Pin	8-36 4-Pin	
Electrical Connection Position	Side	Side	
Mounting	Adhesive	Adhesive	
CE [4]			
SUPPLIED ACCESSORIES: Model 034K10 Cable 10FT Mini 4 Pin To (3) BNC (1) Model 080A100 Petro Wax (1) Model 080A90 Quick Bonding Gel (1) Model ACS-1T NIST traceable triaxial amplitude response, 10 Hz to upper 5% frequency. (1)			
Entered: AP	Engineer: JJB	Sales: WDC	Approved: JJB
Date: 11/8/2013	Date: 11/8/2013	Date: 11/8/2013	Date: 11/8/2013
			Spec Number: 10463
PCB PIEZOTRONICS™ 3425 Walden Avenue, Depew, NY 14043		Phone: 716-684-0001 Fax: 716-684-0987 E-Mail: info@pcb.com	

Model Number	TRIAxIAL ICP® ACCELEROMETER		Revision: D
366A25			ECN #: 25024
Performance	ENGLISH	SI	OPTIONAL VERSIONS
Sensitivity (± 10 %)	± 25 mV/g	2.6 mV/(m/s ²)	Optional versions have identical specifications and accessories as listed for the standard model except where noted below. More than one option may be used.
Measurement Range	± 200 g pk	± 1960 m/s ² pk	HT - High temperature, extends normal operation temperatures [3]
Frequency Range (± 5 %)	1 to 5000 Hz	1 to 5000 Hz	Excitation Voltage
Frequency Range (± 10 %)	0.5 to 6500 Hz	0.5 to 6500 Hz	23 to 30 VDC
Resonant Frequency	± 25 kHz	± 25 kHz	Output Bias Voltage
Broadband Resolution (1 to 10,000 Hz)	0.0002 g rms	0.002 m/s ² rms	7 to 16 VDC
Non-Linearity	± 1 %	± 1 %	2 to 5000 Hz
Transverse Sensitivity	± 5 %	± 5 %	1.4 to 6500 Hz
Environmental			Broadband Resolution (1 to 10,000 Hz)
Overload Limit (Shock)	± 7000 g pk	± 68,600 m/s ² pk	0.0003 g rms
Temperature Range (Operating)	-65 to +250 °F	-54 to +121 °C	0.003 g rms
Temperature Response	See Graph	See Graph	Temperature Range (Operating)
Base Strain Sensitivity	0.001 g/μs	0.01 (m/s ²)/μs	-65 to +325 °F
Electrical			-54 to +163 °C
Excitation Voltage	20 to 30 VDC	20 to 30 VDC	Discharge Time Constant
Constant Current Excitation	2 to 20 mA	2 to 20 mA	0.1 to 0.6 sec
Output Impedance	≤ 100 ohm	≤ 100 ohm	Spectral Noise (1 Hz)
Output Bias Voltage	8 to 12 VDC	8 to 12 VDC	190 μg/√Hz
Discharge Time Constant	0.5 to 2.0 sec	0.5 to 2.0 sec	Spectral Noise (10 Hz)
Setting Time (within 10% of bias)	<5 sec	<5 sec	147 (μm/s ²)/√Hz
Spectral Noise (1 Hz)	70 μg/√Hz	686 (μm/s ²)/√Hz	Spectral Noise (100 Hz)
Spectral Noise (10 Hz)	15 μg/√Hz	147 (μm/s ²)/√Hz	5 μg/√Hz
Spectral Noise (100 Hz)	3 μg/√Hz	29.4 (μm/s ²)/√Hz	Spectral Noise (1 kHz)
Spectral Noise (1 kHz)	2 μg/√Hz	19.6 (μm/s ²)/√Hz	3 μg/√Hz
Physical			Spectral Noise (1 kHz)
Sensing Element	Ceramic	Ceramic	2 μg/√Hz
Sensing Geometry	Shear	Shear	
Housing Material	Titanium	Titanium	
Sealing	Hermetic	Hermetic	
Size (Height x Length x Width)	0.55 in x 0.80 in x 0.55 in	14.0 mm x 20.3 mm x 14.0 mm	
Weight	0.37 oz	10.5 gm	
Electrical Connector	1/4-28 4-Pin	1/4-28 4-Pin	
Electrical Connection Position	Side	Side	
Mounting Thread	10-32 Female	10-32 Female	
Mounting Torque	10 to 20	113 to 225	
			NOTES:
			[1] TEDS option adds 1.0 VDC to bias voltage.
			[2] Typical.
			[3] Valid from +250 to +325 °F (+121 to +163 °C), with HT option only.
			[4] Zero-based, least-squares, straight line method.
			[5] See PCB Declaration of Conformance PS023 for details.
			SUPPLIED ACCESSORIES:
			Model 080A109 Petro Wax (1)
			Model 080A12 Adhesive Mounting Base (1)
			Model 081B05 Mounting Stud (10-32 to 10-32) (1)
			Model ACS-11 NIST traceable triaxial amplitude response, 10 Hz to upper 5% frequency. (1)
			Model M081B05 Mounting Stud 10-32 to M6 X 0.75 (1)
			Entered: <u>BJS</u> Engineer: <u>ALB</u> Sales: <u>WDC</u> Approved: <u>EB</u> Spec Number:
			Date: <u>1/10/06</u> Date: <u>1/10/06</u> Date: <u>1/10/06</u> Date: <u>1/10/06</u> 12854
			PCB PIEZOTRONICS Phone: 716-684-0001
			VIBRATION DIVISION Fax: 716-685-3886
			3425 Walden Avenue, Depew, NY 14043 E-Mail: vibration@pcb.com

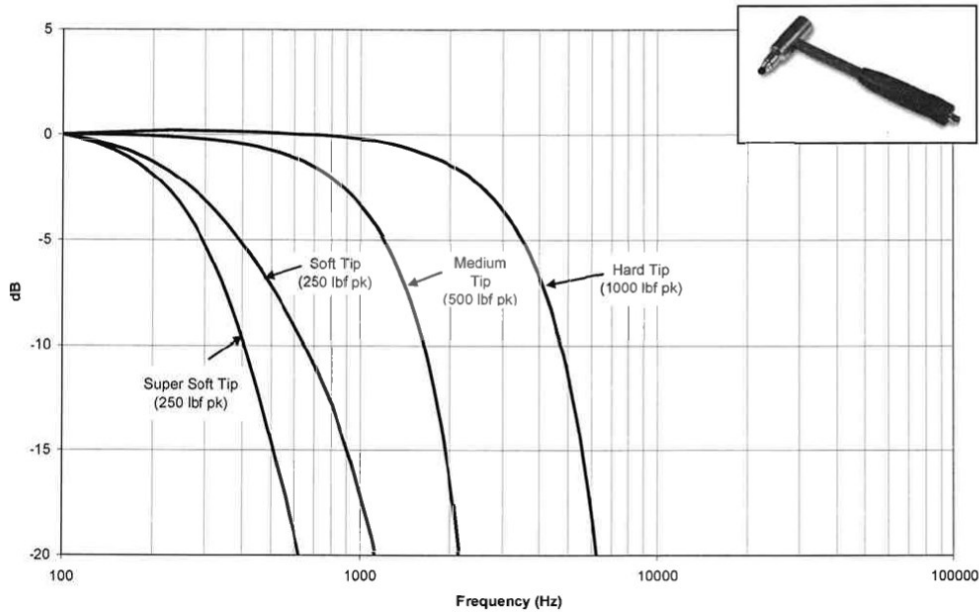


All specifications are at room temperature unless otherwise specified.
 In the interest of constant product improvement, we reserve the right to change specifications without notice.
 ICP® is a registered trademark of PCB Group, Inc.

Model Number	ICP® IMPACT HAMMER		Revision: G
086D20			ECN #: 32971
Performance	ENGLISH	SI	OPTIONAL VERSIONS
Sensitivity (± 15 %)	1 mV/lbf	0.23 mV/N	Optional versions have identical specifications and accessories as listed for the standard model except where noted below. More than one option may be used.
Measurement Range	± 5000 lbf pk	± 22,240 N pk	T - TEDS Capable of Digital Memory and Communication Compliant with IEEE P1451.4
Resonant Frequency	± 12 kHz	± 12 kHz	TLD - TEDS Capable of Digital Memory and Communication Compliant with IEEE 1451.4
Non-Linearity	± 1 %	± 1 %	Output Bias Voltage
Electrical			8.5 to 15 VDC
Excitation Voltage	20 to 30 VDC	20 to 30 VDC	
Constant Current Excitation	2 to 20 mA	2 to 20 mA	
Output Impedance	<100 ohm	<100 ohm	
Output Bias Voltage	8 to 14 VDC	8 to 14 VDC	
Discharge Time Constant	≥ 1400 sec	≥ 1400 sec	
Physical			NOTES:
Sensing Element	Quartz	Quartz	[1] Typical.
Sealing	Hermetic	Hermetic	SUPPLIED ACCESSORIES:
Hammer Mass	2.4 lb	1.1 kg	Model 084A60 Tip - super soft plastic, gray (1)
Head Diameter	2.0 in	5.1 cm	Model 084A61 Tip - soft plastic, brown (1)
Tip Diameter	2.0 in	5.1 cm	Model 084A62 Tip - medium plastic, red (1)
Hammer Length	14.5 in	37 cm	Model 084A63 Tip - hard plastic, black (1)
Electrical Connection Position	Bottom of Handle	Bottom of Handle	Model HCS-2 Calibration of Series 086 instrumented impact hammers (1)
Electrical Connector	BNC Jack	BNC Jack	
			Entered: <u>JH</u> Engineer: <u>BAN</u> Sales: <u>WDC</u> Approved: <u>EB</u> Spec Number:
			Date: <u>5/20/10</u> Date: <u>5/12/10</u> Date: <u>5/12/10</u> Date: <u>5/14/10</u> 12923
			PCB PIEZOTRONICS Phone: 716-684-0001
			VIBRATION DIVISION Fax: 716-685-3886
			3425 Walden Avenue, Depew, NY 14043 E-Mail: vibration@pcb.com

All specifications are at room temperature unless otherwise specified.
 In the interest of constant product improvement, we reserve the right to change specifications without notice.
 ICP® is a registered trademark of PCB Group, Inc.

086D05 Family Impulse Hammer Response Curves



LMS SCADA III

SC316 mainframe

- Number of slots: 16
- Interface: SCSI
- Power: auto ranging $88V_{AC}$ to $264V_{AC}$
- Dimensions: 448mm (19") x 183mm (4U) x 461mm
- Includes master/slave interface

SC317 slave unit

- Number of slots per frame: 17
- Dimensions: as SC316
- Total number of slots in master/slave system: 240 max

SC309EC mainframe with embedded computer

- Number of slots: 9
- Embedded state-of-the-art PC with 1280x1024 graphics controller, Ultra DMA hard disk, floppy disk, 2 serial ports, parallel port, and external SCSI connection for peripherals
- Power and dimensions: as SC316
- Includes master/slave interface

SC310/SC310DC compact mainframe

- Number of slots: 10
- Dimensions: 336mm (3/4 19") x 183mm (4U) x 461mm
- Power: auto ranging $88V_{AC}$ to $264V_{AC}$
- Additional wide range DC power input available on SC310DC
- Optional master/slave interface available

PQA, 4 channel voltage amp

- Input coupling: DC, AC, ICP
- Input range: from $\pm 62.5mV$ to $\pm 10V$
- Includes analog A-weighting filter, overload detection and ICP check

PQFA, 4 channel floating amp

- Input coupling: DC, AC, ICP in single ended or floating mode
- Input range: from $\pm 62.5mV$ to $\pm 10V$
- High-pass filter: 2-pole with cut-off from 5Hz to 75Hz
- Includes overload detection, ICP check and TEDS interface

PQCA, 4 channel charge amp

- Input coupling: charge
- AC coupling: 0.5Hz and 5Hz
- Input range: from $\pm 25pC$ to $\pm 51200pC$

PQMA, 4 channel microphone amp

- Input coupling: AC, DC, ICP, MIC
- Input range: from $\pm 10mV$ to $\pm 25V$
- Microphone supply: 0V or 200V polarization, $\pm 28V$ pre-amplifier supply
- High-pass filter: 2-pole with cut-off from 5Hz to 75Hz
- Includes overload detection and ICP check

PQBA: 4 channel bridge amp

- Input coupling: DC
- Input range: from $\pm 1mV$ to $\pm 1V$
- Bridge configuration: full, half and quarter bridge
- Bridge completion: 120W and 350W
- Balancing: by current injection

SP90: 4 channel ADC/DSP

- ADC: 16-bit $\Sigma\Delta$, 204.8kHz sampling per channel
- Analog anti-alias filter: 5 pole ETD
- Bandwidth: 90kHz maximum
- Processing functions: decimation filters, digital AC coupling, order tracking, third octave, RMS and absolute maximum

QDAC: 4 channel output module

- DAC: 24bit bitstream
- Bandwidth: 20kHz maximum
- Output functions: random, sine, stepped sine, chirp, burst, user

DDAC: 2 channel output module

- As QDAC but with 2 output channels

VDAC: 2 channel output for VIBCO and durability applications

- DAC: 18-bit
- Attenuator: 0-80dB
- Bandwidth: 20kHz maximum
- Protection: slow shutdown at power-fail or external command
- Output functions: random, sine, stepped sine, burst, user

PDT: 2 channel tacho module

- Tacho input: autoranging differential
- Counter clock: 26MHz
- Pre-view: via 2 on-board ADC's

